PLOS BIOLOGY

RESEARCH ARTICLE

Notch dimerization and gene dosage are important for normal heart development, intestinal stem cell maintenance, and splenic marginal zone B-cell homeostasis during mite infestation

Francis M. Kobia[1☯¤], **Kristina Preusse**[1☯], **Quanhui Dai**[1,2], **Nicholas Weaver**[3], **Matthew R. Hass**[1], **Praneet Chaturvedi**[1], **Sarah J. Stein**[4], **Warren S. Pear**[4], **Zhenyu Yuan**[5], **Rhett A. Kovall**[5], **Yi Kuang**[1], **Natanel Eafergen**[6], **David Sprinzak**[6], **Brian Gebelein**[1], **Eric W. Brunskill**[1], **Raphael Kopan**[1]*

1 Division of Developmental Biology, Department of Pediatrics, University of Cincinnati College of Medicine and Cincinnati Children's Hospital Medical Center, Cincinnati, Ohio, United States of America, 2 State Key Laboratory of Genetic Engineering, School of Life Sciences, Fudan University, Shanghai, China, 3 Immunology Graduate Program, University of Cincinnati College of Medicine, Cincinnati, Ohio, United States of America, 4 Department of Pathology and Laboratory Medicine, Abramson Family Cancer Research Institute, Perelman School of Medicine at the University of Pennsylvania, Philadelphia, Pennsylvania, United States of America, 5 Department of Molecular Genetics, Biochemistry and Microbiology, University of Cincinnati College of Medicine, Cincinnati, Ohio, United States of America, 6 School of Neurobiology, Biochemistry, and Biophysics, The George S. Wise Faculty of Life Sciences Tel Aviv University, Tel Aviv, Israel

☯ These authors contributed equally to this work.
¤ Current address: Mount Kenya University, Department of Research and Innovation, Thika, Kenya
* Raphael.Kopan@CCHMC.ORG

Abstract

Cooperative DNA binding is a key feature of transcriptional regulation. Here we examined the role of cooperativity in Notch signaling by CRISPR-mediated engineering of mice in which neither Notch1 nor Notch2 can homo- or heterodimerize, essential for cooperative binding to sequence-paired sites (SPS) located near many Notch-regulated genes. Although most known Notch-dependent phenotypes were unaffected in Notch1/2 dimer–deficient mice, a subset of tissues proved highly sensitive to loss of cooperativity. These phenotypes include heart development, compromised viability in combination with low gene dose, and the gut, developing ulcerative colitis in response to 1% dextran sulfate sodium (DSS). The most striking phenotypes—gender imbalance and splenic marginal zone B-cell lymphoma—emerged in combination with gene dose reduction or when challenged by chronic fur mite infestation. This study highlights the role of the environment in malignancy and colitis and is consistent with Notch-dependent anti-parasite immune responses being compromised in Notch dimer–deficient animals.

Abbreviations: ANK, Ankyrin repeat; ATAC-seq, Assay for Transposase Accessible Chromatin sequencing; ChIP, chromatin immunoprecipitation; CSL, CBF1/Suppressor of Hairless/LAG-1; D/AM, complementing halves of DAM; DAM, DNA adenine methylase; DHS, DNAse hypersensitive; DN, double negative (CD4$^-$ CD4$^-$) T cells; DP, double positive (CD4$^+$ CD8$^+$) T cells; DSS, dextran sulfate sodium; E, embryonic day; E(spl), enhancer of split; EMSA, electrophoretic mobility shift assay; F0, filial generation 0; FACS, fluorescence-activated cell sorting; FoB, follicular B-cell; FVB, Friend virus B–susceptible strain; H/E, hematoxylin/eosin; HDM, house dust mite; Hes, Hairy and Enhancer of Split; IgG, immunoglobulin G; IgM, immunoglobulin M; ISC, intestinal stem cell; Klf, Krüppel-like factor; LPS, lipopolysaccharide; Maml, Mastermind-like; MZB, marginal zone B-cell; MZP, MZB precursor; N1, Notch1; N1RA, Notch1 Arg^{1974}Ala; N2, Notch2; N2RA, Notch2 Arg^{1934}Ala; NICD, Notch intracellular domain; NRARP, Notch-regulated ankyrin repeat protein; NTC, Notch transcription complex; P, postnatal day; PEST, Pro-Glu-Ser-Thr rich domain; PP, post-permethrin; RBPj, recombinant binding protein for immunoglobulin Kappa j region; SMZL, splenic marginal zone B-cell lymphoma; SP, single positive (CD4$^-$ CD8$^+$ or CD4$^+$ CD$^-$) T cells; SPS, sequence-paired site; T2, type 2 cell; T-ALL, T cell acute lymphoblastic leukemia; Th2, T helper 2; TSS, transcription start site; VSD, ventricular septal defect; WT, wild-type.

Introduction

The evolutionarily conserved Notch receptors and ligands influence metazoan development and adult tissue homeostasis by directly translating an intercellular interaction into intracellular transcriptional outputs that control cell fate, proliferation, differentiation, and apoptosis [1–3]. Mammals possess 4 Notch receptors (N1 to N4) and 5 Delta/Jagged ligands; all of which are Type I transmembrane proteins. The Notch pathway stands out relative to other signaling pathways in lacking signal amplification: Canonical Notch signaling is initiated when a ligand on one cell engages a Notch receptor on a neighboring cell. This interaction unfolds the receptor's juxtamembrane region enabling cleavage by the metalloprotease ADAM10. The truncated, cell-membrane-bound polypeptide is then cleaved by the γ-secretase complex freeing the Notch intracellular domain (NICD), which subsequently translocates into the nucleus [2, 4]. NICD associates with the DNA-binding protein CSL (CBF1/Suppressor of Hairless/LAG-1, also known as recombinant binding protein for immunoglobulin Kappa j region (RBPj) in vertebrates) and recruits the coactivator Mastermind-like (Maml), thereby assembling a Notch transcription complex (NTC) that activates Notch target gene expression [4–6].

The Notch pathway plays complex and context-dependent roles during development and adult tissue homeostasis. Perturbations in the Notch pathway are associated with developmental syndromes [7] and cancers [8, 9]. For example, *Notch1* (N1) promotes T-cell development [10–12], whereas *Notch2* (N2) is indispensable for marginal zone B-cell (MZB) development [13–20]. Accordingly, elevated Notch1 signaling is oncogenic in T cells driving acute lymphoblastic leukemia (T-ALL) [21, 22], whereas increased Notch2 signaling is associated with splenic MZB transformation [23–25]. Inversely, when Notch signals promote differentiation, the pathway can have a tumor suppressor function with diminished Notch signaling being associated with cancer [26, 27].

How can the Notch pathway control multiple, dissimilar outcomes? Because each Notch receptor is consumed as it generates a signal and cannot be reused, signal strength has emerged as a key in controlling outcome. Indeed, some Notch-dependent processes are exquisitely sensitive to dosage and manifest both haploinsufficient and triplomutant effects in tissues such as the fly wing [1, 28]. In mammalian tissues, signal strength, defined as the sum of NICD released from all ligand-bound Notch receptors on the cell surface, is a far more important determinant of Notch signaling outcomes than NICD composition (i.e., N1ICD versus N2ICD) [20, 29, 30]. Several mechanisms have been found to modulate signal strength, including receptor glycosylation [31, 32], force-generating ligand endocytosis [33, 34], the contact interface between cells [35], and the ratio of receptor/ligand constitution within the cell [36]. More recently, ligand-dependent signal dynamics were demonstrated to be another key determinant of signaling outcomes [37].

Interestingly, NICD can assemble into dimeric, cooperative NTCs [38] on sequence-paired sites (SPSs), first described in the regulatory regions of the *Drosophila* enhancer of split [E(spl)] locus [39]. SPSs consist of 2 DNA-binding sites orientated in a head-to-head manner [39, 40] separated by 15–17 nucleotides [41]. NICD dimerization is facilitated via a conserved interface in NICD's ANK (Ankyrin repeat) domain. In human N1ICD, this interface consists of Arg^{1985}, Lys^{1946}, and Glu^{1950}. Dimerization in NOTCH1 is effectively abolished by mutating Arg^{1985} into Ala^{1985} (R^{1985}A), Lys^{1946} into Glu^{1946} (K^{1946}E) or Glu^{1950} into Lys^{1950} (E^{1950}K), and loss of dimerization results in reduced activation of dimer-dependent targets [38, 41, 42].

Given the conservation of the dimer interface in most Notch receptors (*Caenorhabditis elegans* being the exception), the conservation of SPSs near known Notch targets [43–45], and the ability of synthetic SPSs to regulate NICD levels [46], we hypothesized that the precise mixture of agnostic and dimer-sensitive targets in a given cell will couple with Notch signal strength and dynamics to shape the responses to Notch signals and contribute to the context-specificity

of Notch-related pathologies. To test this hypothesis in a mammalian species, we evaluated mice homozygous or hemizygous for dimerization-deficient alleles of *Notch1* ($N1^{RA}$) and *Notch2* ($N2^{RA}$) and found that dimerization contributes to context-specific Notch activity. We report that in the hemizygous state, dimer-deficient Notch molecules are haploinsufficient in the heart and intestine, with lethal consequences when modified by the presence of the ecto-parasite, *Demodex musculi* (fur mites). Mice homozygous for a dimer-deficient $N1^{RA/RA}$ allele displayed a female-biased, mild cardiac phenotype consistent with Notch loss-of-function. Conversely, $N2^{RA/RA}$ mice displayed a striking over proliferation of MZBs in parasite-infested mice but not in mite-free mice. In time, the cell-type specific gain-of-function activity of $N2^{RA/RA}$ produced a splenic marginal zone lymphoma-like phenotype in mite-exposed mice. Mechanistically, these effects are consistent with a shift in target amplitude favoring mono-mer-driven targets and a potential reduction in negative feedback.

Results

Generation of N1 and N2 dimerization-deficient mice

To interrogate the physiological role of dimerization, we first quantified the effective binding cooperativity of NTC to SPS and CSL sites using purified RBPj, the N1 RAM-ANK domain, and a MAML protein in electrophoretic mobility shift assays (EMSAs). We compared the mobility of NTC complexes containing either wild-type (WT) N1ICD or a mutant version with the substitution of a single critical Arginine residue (Arg^{1974}) located in the mouse N1 ANK domain to alanine ([Fig 1A and 1B](#), [S1A–S1D Fig](#)). Quantifying the intensity levels of the bands in the image and fitting the data to a binding model that takes into account cooperative binding (see [methods](#)), we measured the cooperativity contributed by NTC binding to either an SPS probe (1xSPS) or a CSL probe containing 2 sites (2xCSL). We find that both WT and mutant NTC had no cooperative binding to the 2xCSL probe. In contrast, when the first site was already bound, the WT NTC displayed a 5-fold stronger binding to the second site in the 1xSPS probe compared with binding to the first site. Importantly, NTC containing $N1^{RA}$ICD had no cooperative binding to the second site in the 1xSPS probe ([Fig 1A](#), [S1A–S1D Fig](#)). Dimerization-dependent activity of N2ICD and its ability to heterodimerize with N1ICD suggests it too binds cooperatively to SPS ([S1F Fig](#)).

To ask whether loss of cooperativity impacts function in vivo, we used CRISPR-Cas9 to introduce amino acid substitutions at Arg^{1974} and Arg^{1934} in N1 and N2, respectively. Following the generation of a double-strand break in Exon 32 of N1 or N2, a short oligonucleotide harboring 2 linked mutations was homologously recombined. Nucleotides coding for Arg^{1974} in N1 ($N1R^{1974}$) and Arg^{1934} in N2 ($N2R^{1934}$) were changed to code for Ala, creating the $N1^{R1974A}$ ($N1^{RA}$) and $N2^{R1934A}$ ($N2^{RA}$) mutations, respectively ([Fig 1B and 1E](#)). To facilitate genotyping of N^{RA} mice, silent mutations were introduced to abolish a BglII restriction site while creating an XbaI restriction site in $N1^{RA}$ ([Fig 1B](#)) or to generate a BglII restriction site in $N2^{RA}$ ([Fig 1E](#)). Animals that carry 1 ($N1^{+/RA}$ or $N2^{+/RA}$) or 2 ($N1^{RA/RA}$ or $N2^{RA/RA}$) mutated chromosomes were first identified by digesting PCR products of the targeted chromosomal regions in Exon 32 with XbaI and/or BglII. XbaI cuts the $N1^{RA}$ chromosome but not the WT PCR product; BglII cuts the $N2^{RA}$ but not the N2 WT PCR products ([Fig 1D and 1G](#)). The presence of each respective RA mutation in $N1^{RA}$ and $N2^{RA}$ founders was subsequently confirmed by direct DNA sequencing ([Fig 1C and 1F](#)). Animals deficient for N1 dimerization ($N1^{RA/RA}$), N2 dimerization ($N2^{RA/RA}$), or both N1 and N2 dimerization ($N1^{RA/RA}; N2^{RA/RA}$) were generated by crossing founders. All were viable, fertile, and without any overt phenotype at P360 in mixed or C57BL6 background (unless otherwise stated, all subsequent results were generated in the mixed background). Because Notch1 signaling plays a central role in T-cell
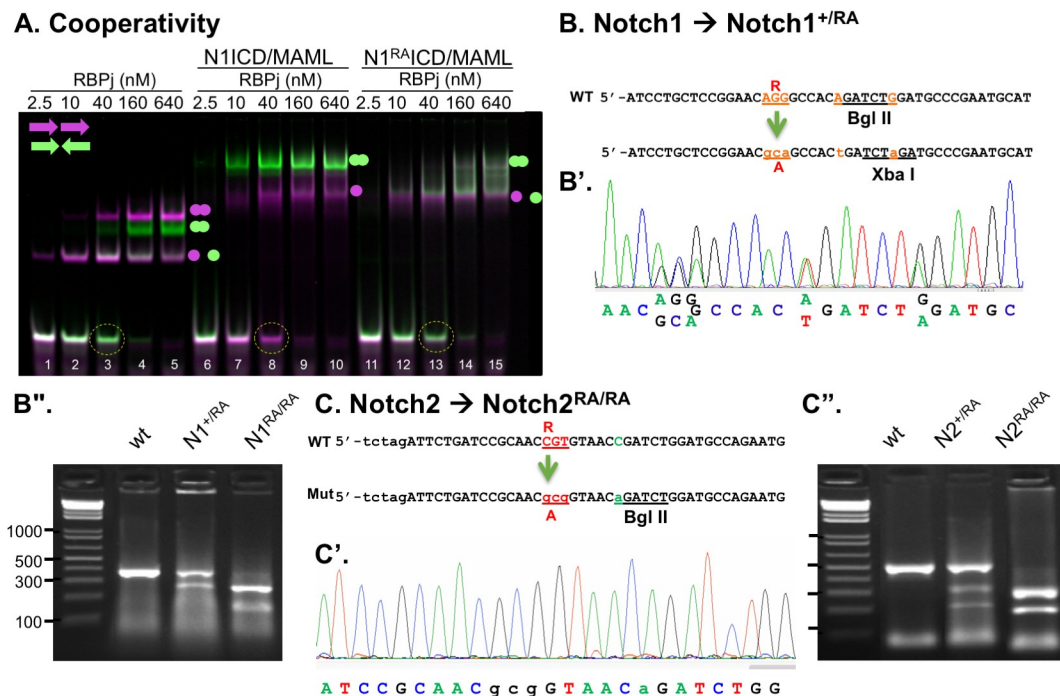
Fig 1. Generation of Notch dimerization-deficient mice. A. Electrophoresis mobility shift assay for purified proteins binding to CSL (magenta) or SPS (green) probes. Balls mark occupancy of 1 or 2 sites. Note that cooperative binding by WT NTC, but not the RA mutant NTC, specifically depletes the SPS probe but not the CSL probe (compare lanes 8 and 13). See text and S1 Fig for detail. **B-C.** CRISPR-Cas9-mediated double-strand break was used to mediate homologous recombination of a short oligonucleotide into Exon 32 substituting Arg $N1^{R1974}$ (**B-B"**) and $N2^{R1934}$ into Ala (**C-C"**), generating $N1^{RA/RA}$ and $N2^{RA/RA}$ animals. To facilitate genotyping, 2 silent mutations (in red) were included in the oligo, abolishing the BglII restriction site while generating an XbaI site in *Notch1* (**B'**). In Notch2, a silent mutation (in green) was included to create a BglII site (**C'**). Sequencing PCR products containing these regions confirmed the presence of the Arg to Ala substitution in founders; digestion of these PCR products with XbaI (for N1, **B"**) and BglII (for N2, **C"**) confirmed the presence of 1 (N1) or 2 (N2) mutant alleles. See S1 Data for raw data. CSL, CBF1/Suppressor of Hairless/LAG-1; MAML, mastermind-like; N1ICD, Notch1 intracellular domain; $N1^{RA/RA}$; $N2^{RA/RA}$, Notch1/Notch2 RA homozygous; NTC, Notch transcription complex; RA, Arg ($N1^{R1974}$/$N2^{R1934}$) to Ala substitution; RBPj, recombinant binding protein for immunoglobulin Kappa j region; SPS, sequence-paired site; WT, wild-type.

https://doi.org/10.1371/journal.pbio.3000850.g001

development [10], we expected that loss of Notch1 dimerization would negatively impact the T-cell compartment. However, an analysis of the T-cell compartments in the thymus and spleen as well as thymic T-cell subcompartments (CD4⁻/CD8⁻ double negative [DN]; single positive [SP], and CD4⁺/CD8⁺ double positive [DP]), revealed a normal T-cell compartment in $N1^{RA/RA}$ mice relative to WT controls (S2 Fig). These findings and the normal life span of $N1^{RA/RA}$ and $N2^{RA/RA}$ animals was surprising because we anticipated many dimerization-dependent genes (e.g., Notch-regulated ankyrin repeat protein [*Nrarp*], *Hes* [Hairy and Enhancer of Split*) 1*, *Hes5*, and *Myc*; [38, 45]) would be negatively impacted as seen when con-stitutively active WT and dimer mutant Notch proteins lacking the extracellular domain (NΔE and N^RA^ΔE) are overexpressed in cell culture (S1E Fig).

Homologous $N1^{RA/RA}$; $N2^{RA/RA}$ mice display barrier defects in the colon and reduced proliferation in the crypt when challenged with 1% DSS

Notch1 and Notch2 act redundantly during the development and maintenance of the gut to block Klf (Krüppel-like factor)4-induced niche exit of intestinal stem cells [47, 48] and Math1-induced differentiation of secretory cells [49, 50]. However, no pathology was revealed

in histological examination of $N1^{RA/RA}$; $N2^{RA/RA}$ intestines. Several studies have shown that a chronic decrease in Notch signaling compromised the intestinal barrier and exacerbated colitis in different mouse models [51–53]. Under the assumption that a compromised barrier may increase sensitivity to dextran sulfate sodium (DSS)-induced colitis, we asked whether intestinal homeostasis and intestinal barrier were robust in $N1^{RA/RA}$; $N2^{RA/RA}$ by exposing mice to DSS. When given 2.5% DSS in their drinking water, WT mice developed colitis, as evident by a mild weight loss, whereas co-housed $N1^{RA/RA}$; $N2^{RA/RA}$ mice exhibited severe weight loss, necessitating euthanizing within 1 week (Fig 2A). To ask if $N1^{RA/RA}$; $N2^{RA/RA}$ mice were
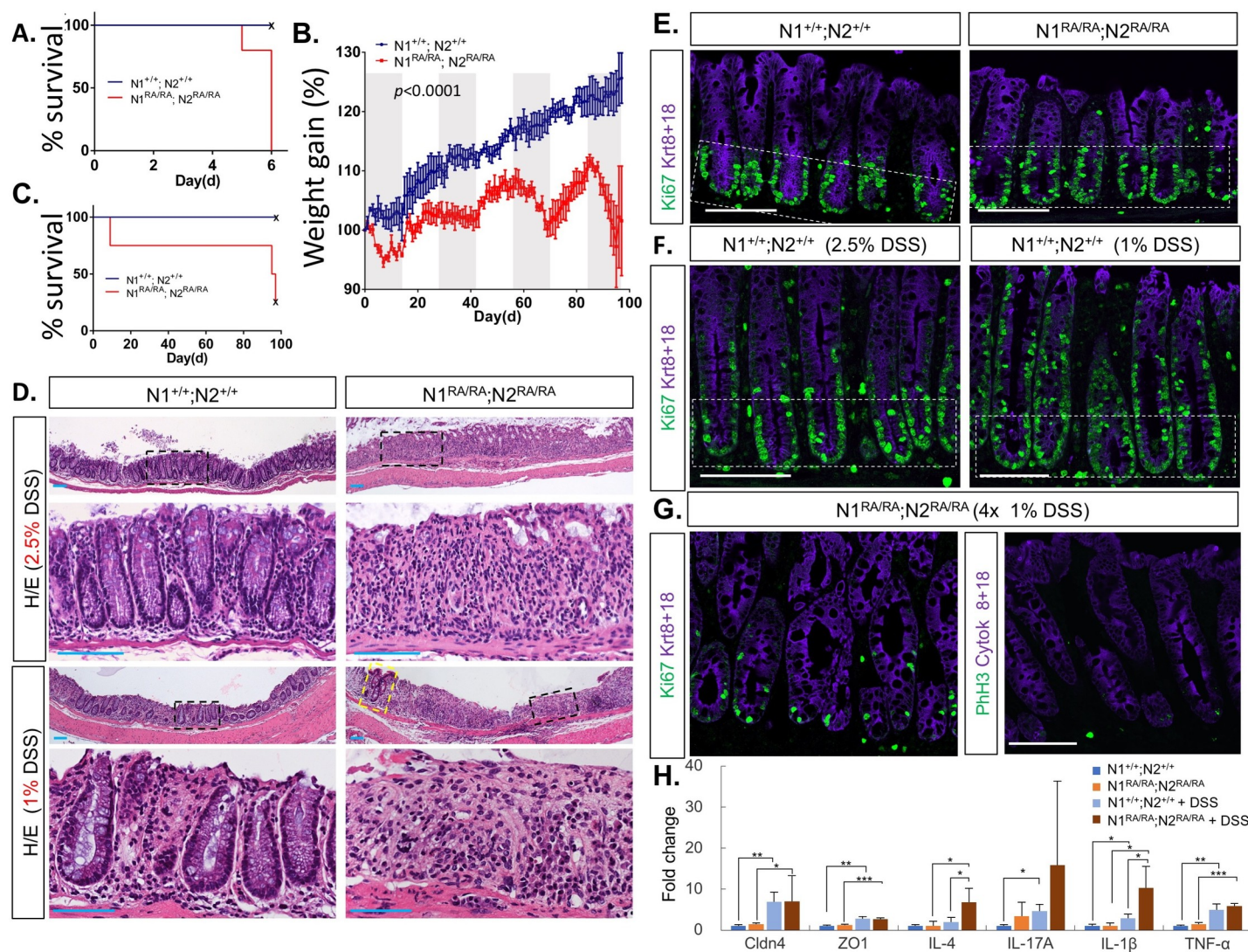
Fig 2. Notch dimerization-deficient mice are sensitized to DSS-induced colitis. A. All $N1^{RA/RA}$; $N2^{RA/RA}$ mice exposed to 2.5% DSS treatment had to be euthanized due to severe weight loss before day 7. **B.** Daily weight measurements of WT (blue) or mutant (red) mice treated with alternate cycles of 1% DSS (gray sections) or no DSS (white sections). **C.** Survival curve of 1% DSS-treated mice. Three of 4 mutant mice had to be euthanized due to severe weight loss by the fourth cycle. **D.** Hematoxylin-eosin staining of colonic tissue from DSS-treated mice. Dashed black boxes are enlarged below. Yellow dashed box showed a section with crypts in an otherwise injured colon in 1% DSS-treated $N1^{RA/RA}$; $N2^{RA/RA}$ mice. **E.** Ki67 staining of untreated mice with the indicated genotypes, crypt regions (Ki67+) are boxed. **F.** Increased proliferation competence in colon of DSS-treated WT mice (Krt8/18+, Ki67+ staining outside the box). **G.** Decreased proliferation competence in colon of $N1^{RA/RA}$; $N2^{RA/RA}$ mice exposed to 4 rounds of 1% DSS. (H) qPCR on RNA extracted from distal colon of $N1^{RA/RA}$; $N2^{RA/RA}$ and WT mice treated for 11 days with 1% DSS; $n = 3$. (*$p < 0.05$), S1 Data for raw data. DSS, dextran sulfate sodium; H/E, hematoxylin/eosin stain; $N1^{RA/RA}$; $N2^{RA/RA}$, Notch1 Arg^{1974}Ala Notch2 Arg^{1934}Ala homozygous qPCR, quantitative polymerase chain reaction; WT, wild-type.

https://doi.org/10.1371/journal.pbio.3000850.g002

predisposed to develop colitis, we exposed them to 1% DSS, which does not affect the weight of control littermates, even after repeated exposures (Fig 2B and 2C). By contrast, co-housed $N1^{RA/RA}$; $N2^{RA/RA}$ mice experienced significant weight loss. Some had blood in their stool at end of the third and fourth DSS cycle, and one had to be removed during the first cycle of DSS following severe weight loss and bloody stool. However, all remaining mice recovered well when DSS was removed from the drinking water, even after multiple cycles of treatment (Fig 2B). Histological analysis of the colons revealed injury in WT mice and a complete disruption of colonic epithelium of $N1^{RA/RA}$; $N2^{RA/RA}$ mice treated with 2.5% DSS (Fig 2D, top). After 4 periods of 1% DSS exposure $N1^{RA/RA}$; $N2^{RA/RA}$ mice had a more severe injury than controls or 2.5% DSS exposed WT mice (Fig 2D). Relative to baseline (Fig 2E), proliferation in WT crypt epithelia (Krt8/18 positive) was elevated in 1% or 2.5% DSS-treated controls (Fig 2F). By contrast, we noticed a surprising decrease in proliferation competence (less Ki67) and mitosis (Phospho-H3 positive cells) in colonic epithelium following the fourth 1% DSS treatment in crypts of $N1^{RA/RA}$; $N2^{RA/RA}$ mice (Fig 2G) relative to WT or untreated crypts, suggesting a role for Notch cooperativity within colonic stem cells recovering from injury. Finally, although RA-specific changes in barrier markers were not detected, an upward trend in IL17a and a significant increase in IL4 and IL1ß was observed in DSS-treated $N1^{RA/RA}$; $N2^{RA/RA}$ relative to WT (Fig 2H), consistent with enhanced inflammatory responses driving colitis in these animals. Thus, these results are consistent with $N1^{RA/RA}$; $N2^{RA/RA}$ alleles being hypomorphic loss-of-function alleles in maintaining intestinal homeostasis and immune response.

$N1^{RA}$; $N2^{RA}$ hemizygotes display impaired intestinal cell proliferation and fate allocation in the crypt and cause ventricular septum defects in the heart

Both the WT and monomeric RA NICD proteins form NTC complexes on CSL sites as shown by EMSA (Fig 1A, S1 Fig) and chromatin immunoprecipitation (ChIP) (S4 Fig in [45]), supporting the hypothesis that the signal generated in $N1^{RA/RA}$; $N2^{RA/RA}$ mice activated sufficient non-SPS gene targets to a level needed to support Notch-dependent decisions. If the Notch RA alleles are hypomorphic, challenging RA mutant mice by lowering protein levels might reveal additional phenotypes. To test this idea, we generated an allelic series in which 1 copy of N1 or N2 was deleted in the $N1^{RA/RA}$; $N2^{+/+}$ or $N1^{+/+}$; $N2^{RA/RA}$ backgrounds, respectively, as well as deleting 1 copy of N1 and 1 copy of N2 in the $N1^{RA/RA}$; $N2^{RA/RA}$ background. Single N1 or N2 RA hemizygotes resembled RA mutants; however, crossing $N1^{RA/RA}$; $N2^{RA/RA}$ with $N1^{+/-}$; $N2^{+/-}$ animals generated significantly fewer $N1^{RA/-}$; $N2^{RA/-}$ pups at birth than expected ($p < 3 \times 10^{-9}$, Chi-squared distribution analysis, S1 Table).

$N1^{+/-}$; $N2^{+/-}$ double hemizygous animals have a normal life span and no overt phenotype under normal housing conditions but have been reported to develop mild cardiac phenotypes [54, 55]. Given the critical role the circulatory system plays during gestation, we suspected that the poor representation of $N1^{RA/-}$; $N2^{RA/-}$ pups at birth was due to defects in cardiac development. Analysis of E16.5 embryos born to mite-free dams revealed highly penetrant and severe ventricular septal defects (VSDs) in the hearts of $N1^{RA/-}$; $N2^{RA/-}$ embryos (Fig 3), consistent with heart defects compromising viability. Milder VSDs were also observed with lower penetrance in $N1^{RA/-}$; $N2^{+/RA}$ embryos (Fig 3). Around this time, the colony became infected with fur mites, but the infestation was not immediately detected on the sentinels. Strikingly, when we retroactively segregated the fecundity data in our colony, we observed a significant ($p = 0.02$, χ^2) skewing of the gender ratio in C57BL6 $N1^{RA/RA}$ carriers, with a male:female ratio nearing 4:1 in fur mite–infested mice, as opposed to the normal 1:1 ratio in mite-free mice (S2 Table).

The longest-lived $N1^{RA/-}$; $N2^{RA/-}$ pup born to mite-infested, mixed-background dams was much smaller than its litter mates and was euthanized at postnatal day 30 (P30) when it
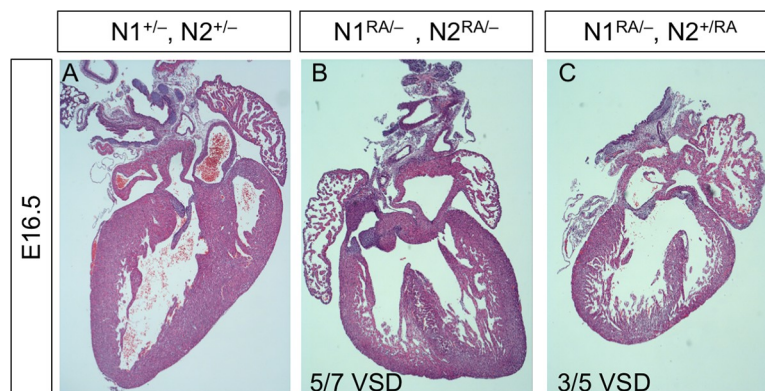
Fig 3. Notch1^{R1974A} substitution compromised ventricular septum development. A. Normal heart with complete septum. **B.** $N1^{RA/-}$; $N2^{RA/-}$ heart with a severe, highly penetrant VSD. The penetrance by age shown below the image. **C.** $N1^{RA/-}$; $N2^{+/RA}$ heart with a milder, less penetrant VSD. E, embryonic day; $N1^{RA/-}$; $N2^{+/RA}$, Notch1 Arg^{1974}Ala Notch2 Arg^{1934}Ala hemizygous; VSD, ventricular septal defect.

became moribund. Necropsy revealed a striking and complete loss of the intestinal crypts and villi [48, 56–58]. Because complete failure to form an intestine would have not permitted survival outside the womb, we assumed this phenotype reflected loss of intestinal stem cells (Fig 4A and 4A'), consistent with the loss of Ki67 in DSS-challenged $N1^{RA/RA}$; $N2^{RA/RA}$ mice (Fig 2G). To investigate this phenotype further, we assessed proliferation and fate allocation in the developing intestine of E18-P1 animals with various allele combinations. To examine fate allocation, we stained sections with Alcian blue and analyzed the number of secretory goblet cells, which are known to expand in Notch hypomorphic backgrounds [50, 56]. The small intestines of control or $N1^{+/-}$; $N2^{+/-}$P0 pups were indistinguishable (Fig 4B and 4C). By contrast, Alcian blue staining revealed a significant expansion in the goblet cell compartment at P0 in $N1^{RA/-}$; $N2^{RA/-}$pups born to fur mite–infested dams (Fig 4D). In mice free of mites, the overall morphology appeared normal with few regions displaying excess goblets. To assess proliferation, we stained adjacent intestinal sections with antibodies against Ki67 and Phospho-H3. Strikingly, whereas trans-hemizygote $N1^{+/-}$; $N2^{+/-}$intestines resembled WT (Fig 4E and 4F), the $N1^{RA/-}$; $N2^{RA/-}$ intestine from mite-infested dames contained very few Ki67 positive cells (Fig 4G and 4H). We also noted a reduction in the number of cells undergoing DNA replication in particular, and competence to self-renew in general, in $N1^{+/-}$; $N2^{RA/RA}$ intestines (S3C, S3C', S3G and S3G' Fig). However, upon eradication of *D. musculi* with permethrin, all E18.5 and all but 1 of 8 surviving P0 $N1^{RA/-}$; $N2^{RA/-}$pups had at least some regions within the small intestine in which Ki67-positive tissue could be observed (Fig 4J, the percentage of Ki67+ crypts; S3I–S3J' Fig; note reduced proliferation in Ki67-positive crypts of a P1 pup post-mite eradication but coinciding with microbiome colonization). Overall, these data reflect an impaired ability to maintain intestinal stem cells in $N1^{RA/-}$; $N2^{RA/-}$mice, which was exacerbated by *D. musculi* infestation. Because these phenotypes can reflect complex interactions between multiple tissues in the $N1^{RA/RA}$; $N2^{RA/RA}$ and $N1^{RA/-}$; $N2^{RA/-}$mice, we deferred the mechanistic analysis of this gene-environment interaction in intestinal stem cells (ISC) maintenance to future investigation.

The $N2^{RA}$ allele drives expansion of MZBs in *D. musculi*–infested mice

MZBs are exquisitely sensitive to *N2* dosage [13–17, 19, 20]. Even a mild reduction in N2ICD can generate a noticeable decline in MZB cell numbers [20]. We used fluorescence-activated cell sorting (FACS) to analyze the splenic B-cell population and asked if $N2^{RA}$ displayed
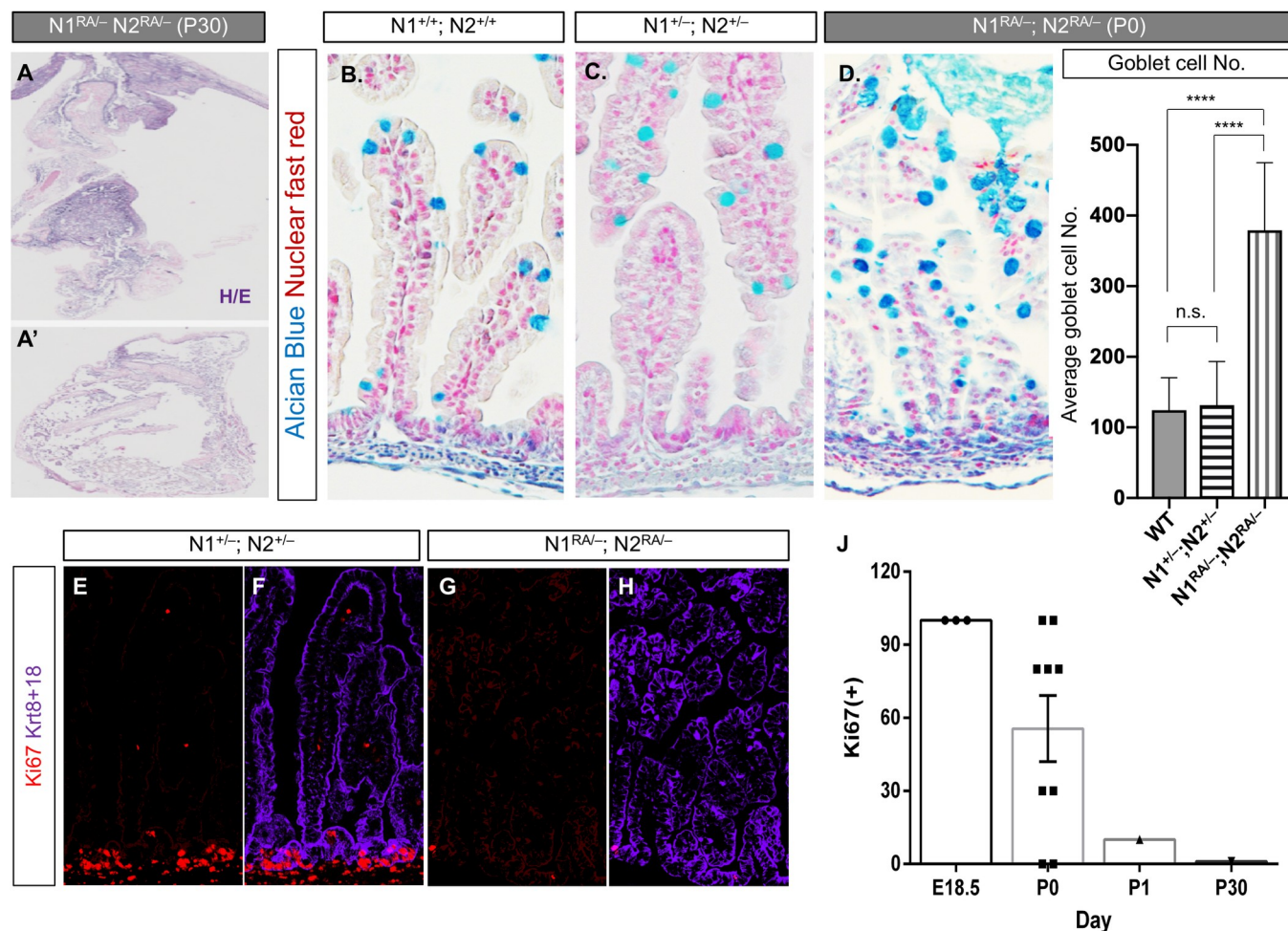
Fig 4. Notch dimerization-deficient mice are hypomorphic for Notch activity in the gut. A. Deletion of one N1 and one N2 allele in the RA background ($N1^{RA/-}$; $N2^{RA/-}$) caused lethality; loss of the intestine (presumably due to stem cell exhaustion) was evident in the longest surviving pup at P30. **B-C.** Alcian blue staining of $N1^{RA/RA}$; $N2^{RA/RA}$ and $N1^{+/-}$; $N2^{+/-}$ adult intestines. **D.** Alcian blue analysis of P0 intestines detected an increase in goblet cell numbers in $N1^{RA/-}$; $N2^{RA/-}$ (E-H) Ki67 staining in P0 intestine from control $N1^{+/-}$; $N2^{+/-}$ (**E, F**) or $N1^{RA/-}$; $N2^{RA/-}$ (**G, H**) newborn. **J.** Quantification of Ki67-positive area at the indicated age, among surviving $N1^{RA/-}$; $N2^{RA/-}$ pups during ($n = 2$) and after ($n = 12$) fur mite infestation; raw data in S1 Data. E, embryonic day; H/E, hematoxylin/eosin stain; $N1^{RA/-}$; $N2^{RA/-}$, Notch1 Arg^{1974}Ala Notch2 Arg^{1934}Ala hemizygous; P, postnatal day; WT, wild-type.

haploinsufficient phenotypes in the dose-sensitive MZ compartment. Intriguingly, we observed a significant increase in the MZB compartment in $N2^{RA/RA}$ spleens in a mixed-background mouse exposed to *D. musculi* (Fig 5A). The size of other splenic B-cell subsets, including the MZB precursors (MZPs), follicular B-cells (FoB) and transitional type-2 cells (T$_2$) did not change significantly in either $N2^{RA/RA}$ (Fig 5A), $N2^{+/-}$ or $N2^{RA/-}$ (Fig 5B), inconsistent with a fate switch.

MZB cells reside in the splenic marginal zone where they surveil for blood-borne pathogens. Upon encountering antigens, they rapidly differentiate into immunoglobulin M (IgM)-producing plasmablasts that secrete vast amounts of IgM before undergoing apoptosis [59]. To test IgM levels in vivo, we performed ELISA on serum collected from unstimulated $N2^{RA/RA}$ and littermate controls and detected no significant difference in the levels of circulating IgM (Fig 5C). To test for the possibility that loss of N2 dimerization negatively impacted differentiation into IgM-producing plasmablasts upon stimulation, we FACS isolated MZB and FoB cells from mite-exposed $N2^{RA/RA}$ and WT spleens. We then stimulated these cells in vitro with
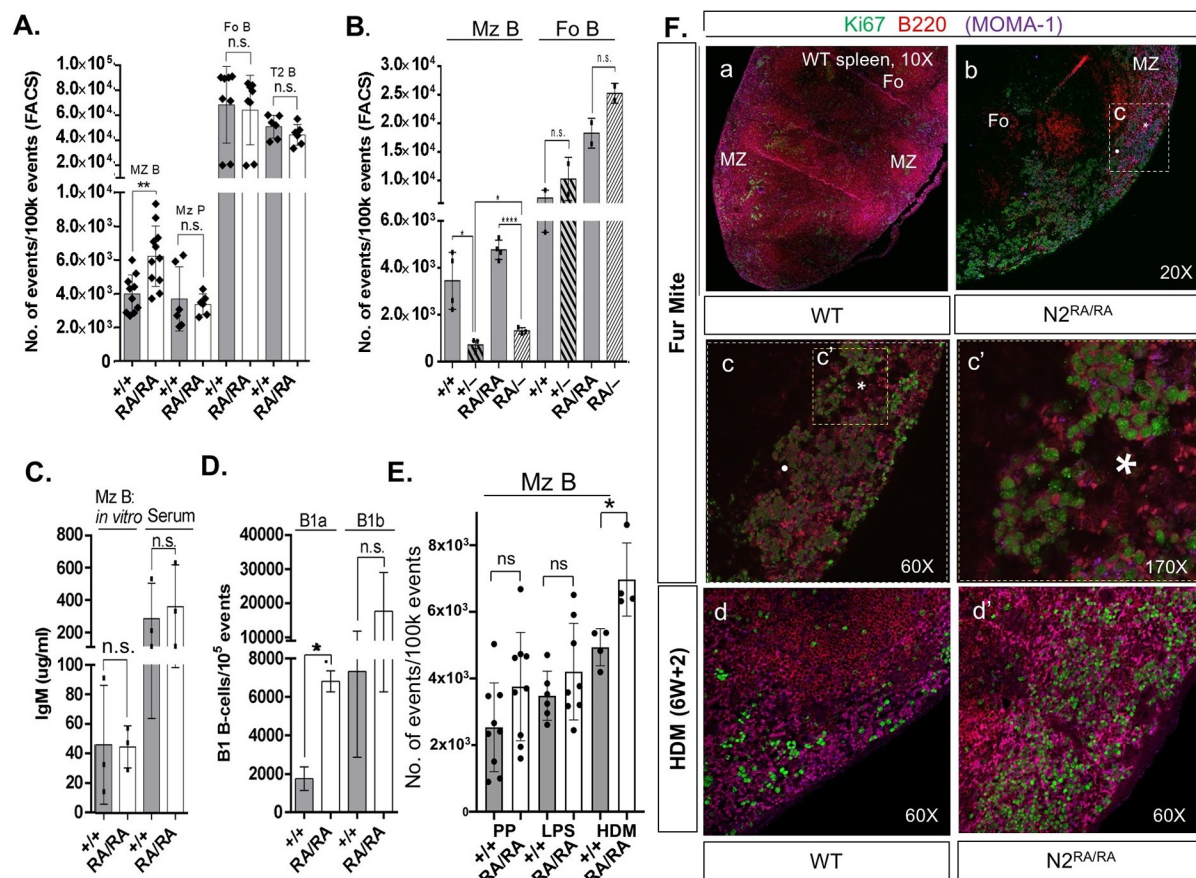
Fig 5. Loss of Notch2 dimerization expands the splenic MZB compartment in the presence of mites. A. FACS analysis of $N2^{RA/RA}$ fur mite–infested mouse spleens revealed an expansion the MZB compartment relative to WT (+/+). Values for MZP, F0, and T_2 splenic B-cell populations were not significantly different; n = 11. **B.** The MZB cell compartment in heterozygotes. **C.** LPS-induced differentiation and IgM production in vitro and serum levels of IgM in vivo; n = 4. **D.** Peritoneal B1a B-cell compartment in mite-infested WT and $N2^{RA/RA}$ mice (n = 2). **E.** The MZB cell compartment in $N2^{RA/RA}$ mice after treatment with permethrin, an immunosuppressant used to manage fur mite infestation (PP), after LPS, or after 6 weeks of treatment with HDM extract. ($^*p < 0.05$). Note, although a slight trend is seen in mite-free animals, power analysis indicates it would take 212 mice displaying this trend to reach significance. For LPS-treated mice, it would take 41 animals displaying this trend to reach significance. Only 4 mice were sufficient to reach significance after treatment with HDM. In (**A-E**) p-values generated by 2-tailed t-test. Error bars represent SD. **F.** Proliferation in the splenic marginal zone of mite-infested mice: (Fa) The spleen from a mite-infested control animal or (Fb) from $N2^{RA/RA}$ mice. Boxed region magnified in Fc and again, in Fc', asterisk and dot provided for orientation. Magnification noted. (Fd, d') 60× view of marginal zone from control and HDM-treated $N2^{RA/RA}$ mice. Raw data in S1 Data. F0, Filial generation 0; FACS, fluorescence-activated cell sorting; FoB, follicular B-cell; HDM, house dust mite; IgM, immunoglobulin M; LPS, lipopolysaccharide; MZB, marginal zone B-cell; $N2^{RA/RA}$, Notch 2 Arg^{1934}Ala homozygous; ns, not significant; P, postnatal day; PP, post-permethrin; T_2, type 2 cell; WT, wild-type.

lipopolysaccharide (LPS) for 5 days followed by imaging to assess for proliferation and by ELISA to quantify the IgM levels secreted into the medium. Relative to WT MZB cells, there was no appreciable difference in the ability of $N2^{RA/RA}$ MZB cells to respond to LPS stimulation (S4A Fig), and ELISA analysis detected no significant difference in the amount of IgM secreted by $N2^{RA/RA}$ MZB cells relative to WT controls (Fig 5C). Finally, we tested whether loss of dimerization affected the development of B1 B cells, which predominantly reside in the peritoneal cavity [16]. Together, these data suggest that MZB cell numbers did not increase because of a fate switch or a failure to differentiate properly and are consistent with a proliferative phenotype triggered by the $N2^{RA}$ mutation. Notably, FACS analysis also revealed a significant expansion of B1a subset of B1 B-cells between $N2^{RA/RA}$ and WT animals but no changes in the levels of the B1b subset (Fig 5D).

In the course of these experiments, the *D. musculi* infestation was eradicated with permethrin. Within a few months, as we saw with other phenotypes, mite-free $N2^{RA/RA}$ animals no longer showed significant MZB expansion (Fig 5E; post-permethrin [PP]). Because permethrin has been reported to suppress the immune system in mice [60, 61], we assumed permethrin transiently suppressed MZB proliferation. Multiple subsequent analyses over many months, however, failed to detect a significant difference in MZB numbers between permethrin-treated $N2^{RA/RA}$ and control mice post eradication, suggesting that this allele was indistinguishable from WT in untreated and pathogen-free animals. Accordingly, we compared MZB numbers between $N2^{+/-}$ spleens (which have decreased MZB numbers due to haploinsufficiency) with $N2^{RA/-}$ spleens and found no further reduction in MZB numbers [13, 20]. These data suggest that the $N2^{RA}$ allele has neither a haploinsufficient character for the $N2^{RA}$ allele in the MZB lineage (Fig 5B) nor a proliferative phenotype triggered cell-autonomously by the $N2^{RA}$ protein. To ask whether environmental stimuli interacted with $N2^{RA}$ within the spleen, mice were exposed to bacterial lipopolysaccharide (LPS) or to dermatitis, produced by twice weekly exposure of the ear epidermis to house dust mite extract (HDM, *Dermatophagoides farinae*) for 6 weeks (see Methods). MZB numbers were analyzed 8 weeks after the first LPS injection or HDM extract application. LPS-induced transient IgM production but did not significantly change MZB census in the spleen at 8 weeks (Fig 5E, note a trend towards increase was observed in the $N2^{RA}$ LPS-treated mice). Importantly, HDM-induced dermatitis elevated MZB numbers only in the $N2^{RA/RA}$ mice but not in controls (Fig 5E, HDM). Collectively, these experiments establish that specific gene-environment interactions produce the MZB phenotype in $N2^{RA/RA}$ mice.

To assess the rate of splenic B-cell proliferation in mite-infested mice, we stained C57BL/6J $N2^{RA/RA}$ and WT (WT) spleen sections with antibodies against Ki67, B220 (to mark the B-cells), and Moma-1 (to mark the marginal zone). We detected defuse B220 staining with elevated Ki67 in marginal zone cells in the $N2^{RA/RA}$ spleen (Fig 5F), as well as in germinal centers (rich in FoB cells and strongly B220 positive, S4 Fig), not seen in WT spleen of co-housed animals (S4B–S4D Fig). Increased marginal zone proliferation in $N2^{RA/RA}$ relative to WT controls was also detected in spleens after 6 weeks of HDM treatment (Fig 5F, 5D and 5D'). Combined, these data suggest that mite infestation or prolonged HDM exposure lead to enhanced MZB proliferation.

Aged $N2^{RA/RA}$ mice have enlarged spleens but only *D. musculi*–infested mice progress to a splenic MZB lymphoma–like state

As noted here, we observed no change in life span in $N2^{RA/RA}$ or $N1^{RA/RA}$; $N2^{RA/RA}$ animals. However, as old animals were culled, we noticed enlarged spleens in animals carrying the $N2^{RA/RA}$ allele post mite eradication (S5A Fig). Spleens from mice infested by *D. musculi* were much larger, the most severe splenomegaly exhibited by $N2^{RA/RA}$; $N1^{+/RA}$ (Fig 6A–6E), perhaps because they contained a higher contribution of the inflammation-prone Friend virus B–susceptible (FVB) strain [62, 63]. Histologically, spleens from mite-infested $N2^{RA/RA}$ carriers lost their typical architectures with $N2^{RA/RA}$; $N1^{+/RA}$ spleens showing the greatest disruption. Splenic morphology showed an expansion of the white pulp at the expense of the red pulp. In the most severe cases, the spleens appeared to consist of white pulp only (Fig 6F–6K). In addition, 2 $N2^{RA/RA}$; $N1^{+/RA}$ animals had multiple enlarged abdominal lymph nodes. H/E staining revealed a striking morphological similarity to the enlarged spleens from the same animals, suggesting infiltration by a splenic population, or lymphoproliferation within the LN (Fig 6L–6L"). To further characterize the nodes, we stained the enlarged spleens and lymph nodes for the B-cell markers B220 and Pax5. Both were positive for the B-cell markers (Fig 6M–6N').
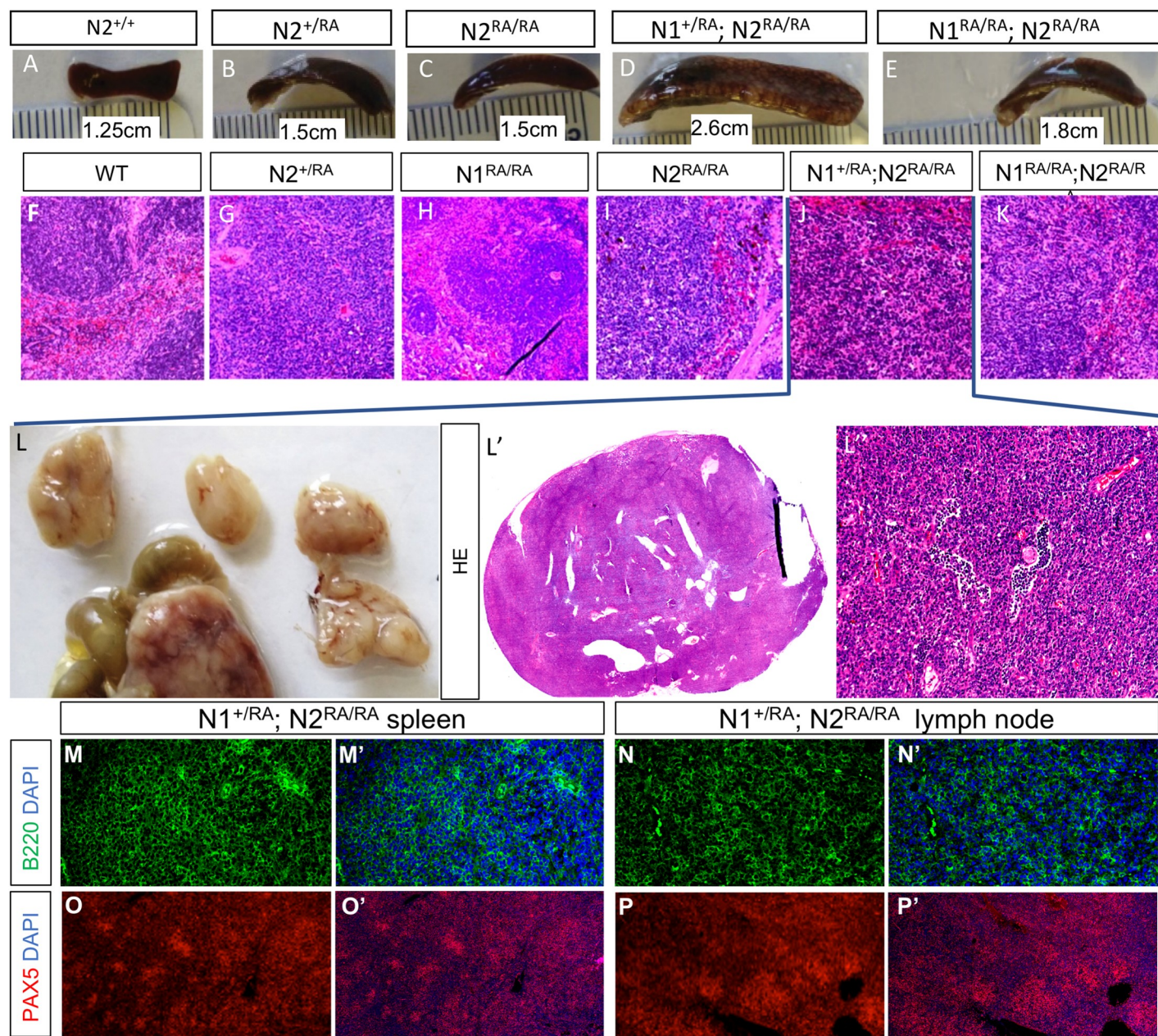
Fig 6. Aged *N2^{RA/RA}* and *N2^{RA/RA; N1+/RA}* mice develop severe splenomegaly and tumors reminiscent of SMZL. A-E. Images of spleens from mice P600-P700 with indicated genotypes. **F-K.** Severely enlarged spleens are associated with disorganized morphology and the appearance of cells with large nuclear:cytoplasmic ratio (genotypes indicated, see low magnification image in S6E Fig). **L.** Large enteric lymph nodes detected in the individual shown in (**J.**), densely populated with cells with large nuclear:cytoplasmic ratio (**L'-L".**). Staining the spleen (**M.**) and lymph node (**N.**) with Ki67 and the B-cell markers B220 and Pax5 identifies infiltrating cells as spleen-derived B cells. Magnification: 10×. *N2^{RA/RA; N1+/RA}*, Notch1/Notch2 RA homozygous; RA, Arg (*N1^{R1974}/N2^{R1934}*) to Ala substitution; SMZL, splenic marginal zone B-cell lymphoma.

These features are reminiscent of human splenic MZB lymphoma (SMZL), a clonal B-cell neoplasm that manifests itself in elderly patients and consists of small lymphocytes that infiltrate the lymph nodes and other organs [23–25]. As would be expected, the enlarged lymph nodes and spleens were highly proliferative as indicated by Ki67 and phospho-H3 staining (S5B and S5D Fig). Paradoxically, human SMZL has been associated with hyperactive NOTCH2 signaling due to an N2ICD-stabilizing truncation upstream to the WSSSP sequence in the Pro-Glu-

Ser-Thr–rich (PEST) domain of NOTCH2 [64–66], whereas the $N2^{RA}$ alleles are hypomorphic in expression assays and in the context of the heart, crypt, and gut barrier. To confirm that this line of CRISPR-modified mice did not inherit a truncated *Notch2* allele, we sequenced Exon 34 DNA isolated from lymph node filled with B-cells and found a perfect match to the WT *Notch2* allele (ENSMUSG00000027878).

Recently, we identified an unanticipated consequence of increasing the number of SPS sites in the *Drosophila* genome, namely, accelerated degradation of phospho-NICD [46]. Further, we demonstrated that this enhanced degradation affects some, but not all, Notch-dependent decisions in *Drosophila*. Bristle precursor cells requiring a pulse of Notch were refractory to the destabilizing effect, whereas wing margin cells reliant on prolonged Notch signals were sensitive to NICD degradation [46]. To test whether the similarity of our phenotype to SMZL might in part be reflective of N2ICD stabilization, we assessed N2ICD levels in nuclear extracts from WT and $N2^{RA/RA}$ MZB cells. Although we see high variability between replicates, we find no evidence for a significant accumulation of nuclear N2ICD in sorted $N2^{RA/RA}$ MZBs (S6 Fig). These findings suggest that the gain-of-function phenotypes observed in $N2^{RA/RA}$ MZB cells are not due to enhanced N2ICD stabilization. Thus, unlike stabilization seen in many human SMZL patients, increased N2ICD stability is unlikely to be the cause of the SMZL phenotype in the $N2^{RA/RA}$ mice.

Loss of Notch dimerization does not impact chromatin accessibility

In $N2^{RA/RA}$ mice, Notch pathway activity in T cells and skin is intact, as it relies on *Notch1*. Assuming the MZB effect is cell autonomous, we asked if the mechanism involved in enabling a haploinsufficient allele to drive MZB expansion involves changes in chromatin accessibility. We performed ATAC-Seq on MZB cells isolated from WT and $N2^{RA/RA}$ mice in the absence of fur mites (4 biological replicates each). We mapped reads under the peaks and used EdgeR (https://bioconductor.org/packages/release/bioc/html/edgeR.html) to identify differential accessibility across the genome between samples (see Methods for details). A total of 89,059 peaks were mapped, of which 87,575 were present in both $N2^{RA/RA}$ and WT MZB cells with all 8 samples being highly related ($R > 92\%$; Spearman Correlation; Fig 7A). Hence, genome accessibility changed minimally between these MZB cells with only 984 peaks (1.1%) enriched in $N2^{RA/RA}$ and 500 (0.56%) in wild type. We next used GREAT to assign genes to all peaks. Based on these assignments, only 108 were unique to WT, and 122 were unique to $N2^{RA/RA}$. Importantly, none of the differently enriched peaks were present at the *Myb* or *FoxM1* loci, which are known to drive of B-cell proliferation [67] or next to a known Notch target *Dtx1* [13] (Fig 7B). Next, we analyzed DNAse hypersensitive peak upstream of the *Myb* locus in the ENCODE datasets and identified an enhancer accessible in several cell types, including the kidney. The genome of a kidney-derived cell line used to overexpress constitutively active NΔE and a dimer-deficient version, NΔERA (S1 Fig) was examined by SplitDamID [45]. We detected strong binding to the *Myb* enhancer using Notch/RBP complementing pairs but not by Notch dimers. These data suggest that the *Myb* enhancer can respond to monomeric NTC and is insensitive to loss of dimeric NTC activity. Collectively, these data suggest that the changes in MZB gene expression in the $N2^{RA/RA}$ animals are not due to changes in chromatin accessibility but may reflect changes in gene expression caused by the loss of Notch dimer NTC complexes at some other loci, most likely the SPS-dependent negative regulators *Hes1*, *Hes5*, and *Nrarp* [45, 68].

Discussion

The possibility that DNA-binding site architecture contributes to Notch signaling outcomes has been considered in past studies [43, 44]. NTCs can bind to enhancers with CSL binding sites as monomers that function independently of one another. In such a model, the
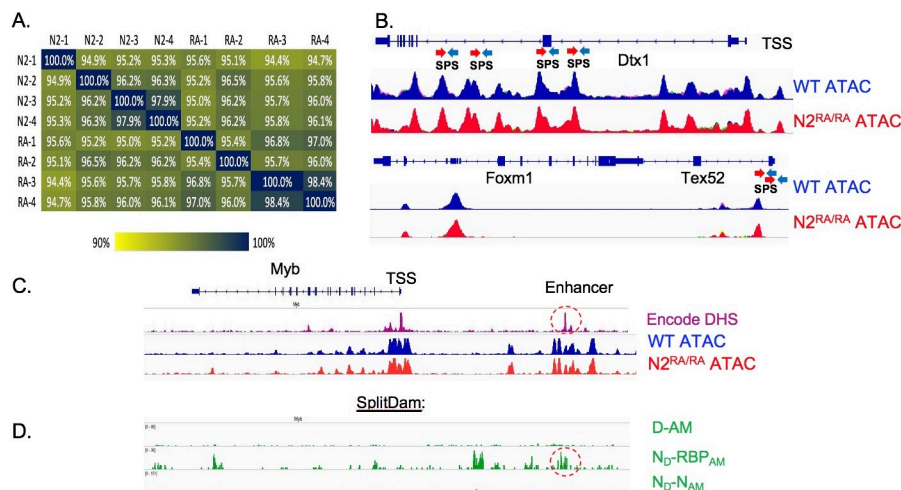
Fig 7. Mite-infested $N2^{RA/RA}$ activate a proliferation module in MZB. A. Spearman correlation table measures ATAC-Seq peaks similarity matrix between 8 mice (4 in each genotype). All are >92% similar. **B-C.** ATAC-Seq data reveal that DNA accessibility was not altered near the Notch target *Dtx1* that is down-regulated in expression in $N2^{RA/RA}$ animals (**B.**). WT in blue, $N2^{RA/RA}$ in red. Location of validated enhancers containing SPSs are shown. Note, each dimer-dependent site can be composed of either 2 canonical sites (red arrows) or 1 canonical and 1 noncanonical site (blue arrow). Close inspection of ATAC peaks and the proliferation drivers *FoxM1i* (**B.**) or *Myb* (**C.**) loci. **D.** The *Myb* locus was analyzed for chromatin accessibility (Encode DHS and ATAC-seq data generated in this study) and DNA methylation by DAM methyl transferase complementation (SplitDAM). The methylation patterns generated by control D/AM halves are compared to methylation patterns generated by Notch-D/RBPj-AM pairs (which recognizes both dimer-dependent and dimer-independent sites) and Notch-D/Notch-AM pairs (which recognizes only dimer-dependent sites). See text and [45] for additional details. ATAC-Seq, Assay for Transposase Accessible Chromatin sequencing; D/AM, complementing halves of DAM; DAM, DNA adenine methyltransferase; DHS, DNAse hyper sensitive; MZB, marginal zone B-cell; $N2^{RA/RA}$, Notch-D, Notch1 fused to the D half of DAM; Notch2 Arg $N2^{R1934}$ to Ala substitution, homozygous; RBPj-AM, recombinant binding protein for immunoglobulin Kappa j region fused to AM half of DAM; SPS, sequence-paired site; TSS, transcription start site; WT, wild-type.

probability of target activation will depend upon the relative abundance of nuclear NICD and the number of CSL sites at a given enhancer [69–71] and/or burst size [72, 73]. SPSs are found in enhancer regions of up to 30% of mammalian Notch targets including *Nrarp/NRARP*, *Hes1/ HES1*, *Hes5*, and *Myc* [30, 38, 42, 74] We have previously documented that approximately 2,500 SPSs were bound by N1ICD dimers in the mouse genome and that dimerization-deficient Notch molecules bind poorly to SPSs in vivo, even at high NICD concentrations [45]. In the murine kidney cell line, mK4, about 15% of Notch targets required NICD dimerization. SPSs and cooperativity also proved critical for the oncogenic activity of N1ICD in murine T cells, where NICD dimerization at a distant enhancer was required for *Myc* activation [42]. Thus, Notch targets are either agnostic to dimerization or sensitive to its presence, leading to the hypothesis that cooperativity may modulate Notch responses at physiological NICD concentrations. Recently, evidence that SPSs contribute to an increased probability of transcriptional activation and increased transcriptional burst duration during *Drosophila* embryonic development was reported [72].

Although our study concludes that embryonic development in the mouse proceeds normally in the presence of Notch receptors lacking cooperativity, it nonetheless uncovered important contributions of cooperativity to mammalian development and homeostasis under environmental stress. Notch^{RA} phenotypes are greatly enhanced by reduced gene dosage in *Notch1*, which causes VSDs ([75–77]) or in both *Notch1* and *Notch2* in the gut. The developmental phenotype uncovered when $N1^{RA}$ dose is reduced (in $N1^{RA/-}$) resembles other Notch pathway deficiencies known to cause a wide range of heart defects, including VSDs, and are

milder than a weak hypomorphic Notch1/2 allele on the B6 background [20]. Interestingly, dosage alone did not impact the ability of the $N2^{RA}$ allele to control development and homeostasis of the dosage-sensitive MZBs in parasite-free mice, even in the hemizygote state ($N2^{RA/-}$).

Strikingly, loss of cooperativity-dependent contributions to homeostasis becomes acute when mutant animals are burdened with exoparasites, namely, fur mites. Interestingly, when the environment includes unmanaged exoparasite infestation, dimerization-deficient cooperativity mutant receptors can behave as hypomorphic (loss-of-function) alleles in some contexts (intestinal barrier formation, ventricular septum formation, intestinal stem cell self-renewal, female survival) yet remain indistinguishable from the WT allele in many other tissues or can trigger a similar disease as a gain-of-function allele (SMZL) in a cell type that otherwise appeared unaffected by the mutation. Note that in $N2^{RA/RA}$ mice, Notch pathway activity in T cells and skin, where $Notch1$ is present, are identical to the WT. Thus, the defect is more likely to reside in the B-cell lineage than elsewhere, although this remains to be examined more fully in the future. We propose these behaviors can be explained by assuming that the balance between targets agnostic to dimerization (like Myb) and those dependent on cooperativity on SPSs (like $Hes1$, $Hes5$, $Nrarp$) varies by cell type (Fig 8). Moreover, these differences in dependence upon SPS versus non-SPS target gene regulation between tissues can be further exposed by additional stressors such as environmental insults (i.e., exoparasites) or changes in gene dose. We propose that accessible SPSs can act as a "sink," holding on to NICDs that otherwise will be available to regulate monomer-dependent enhancers. If true, more $N2^{RA}$ICD may be available to regulate key targets. Importantly, this insight may translate to other transcription factors where variants of uncertain significance are associated with developmental syndromes or neoplastic disease. Such mutations may control molecular behaviors integrating the environment with specific cooperative interactions in affected tissues.
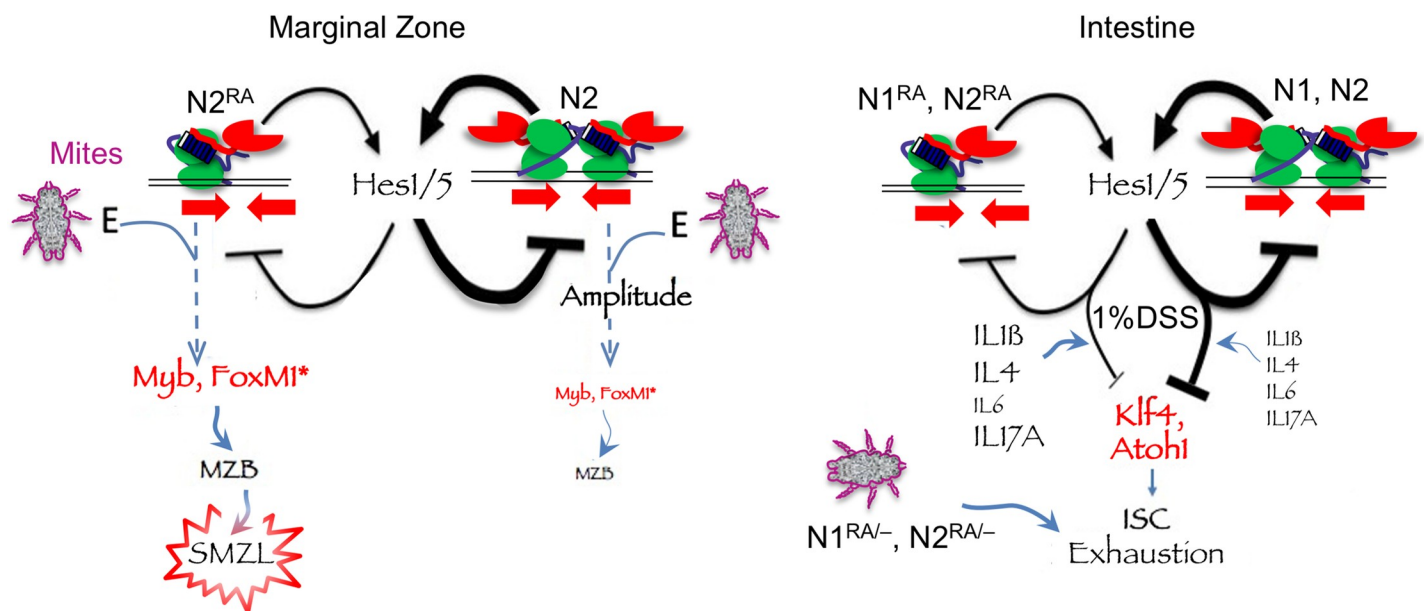
Fig 8. A schematic summary of the findings with a hypothetical mechanism. *Notch* integrates environmental cues (mites, cytokines) to drive proliferation in MZB (*Notch2)* and block differentiation in (ISCs, *Notch*1 and 2). Activation of SPS-dependent *Hes* repressors creates a negative feedback tuning of transcription amplitude in MZB and driving the response magnitude in ISCs. In *Notch$^{RA/RA}$* mutants, SPS-dependent *Hes* gene expression is dampened, and increased availability of NICD^{RA} to monomer-driven target due to reduce trapping on accessible SPS may also contribute. Repeated DSS treatment, or hemizygosity in *Notch$^{RA/RA}$* mutants, exposed insufficient blockade of pro-differentiation signals in ISC, most likely delivered via immune cells or cytokines (IL1ß, 4, or 17A) in DSS-treated mice. Fur mite infestation creates an environment for runaway proliferation in MZB, and enhanced dosage effects in *Notch$^{RA/RA}$* mutants leading to complete loss of ISC postnatally even without DSS challenge. Asterisk marks hypothetical targets selected for their known function in driving B-cell proliferation [67]. DSS, dextran sulfate sodium; ISC, intestinal stem cell; MZB, marginal zone B-cell; NICD, Notch intracellular domain; SMZL, splenic marginal zone B-cell lymphoma; SPS, sequence-paired site.

The diverse cell types responding to a cutaneous parasite must reflect a systemic change driven by the parasite. Because we could replicate the impact on MZB proliferation in short exposures to dust mite extract, live parasite is not needed, and the response is likely mediated by an immune cell (or cytokine) intermediate. Dermatitis is typically associated with both skin-produced cytokines (e.g., IL-33, -17C, and TSLP), and a skewing of CD4+ T cells into T helper 2 (Th2) and their associated cytokines (e.g., IL-4,-5,-13, [78]). Similarly, fur mite infestation has been shown to increase the level of different cytokines (e.g., IL-6 and IL-12; [79] and IL-4 and -5 [80, 81]). Although the exact axis linking anti-parasite immune responses and splenic marginal zone lymphoma, intestinal homeostasis, female/male ratios, and heart development are yet to be identified, this study highlights the role of the environment in chronic disease, including ulcerative colitis and a smoldering malignancy such as SMZL. Combined with the significantly better outcomes in SMZL patients with activated *Notch2* alleles [65], one has to wonder about the role of the immune environment in onset and progression of human SMZL patients with *Notch2* mutations.

Methods

Ethics statement

Mice were housed at CCHMC's animal facility in accordance with IACUC's animal welfare regulations. The use of animals for the experiments described in this work was approved through protocol number IACUC2018-0105.

Animals

To generate the RA alleles, 3 gRNAs (g25, g26, and g27) that target sites surrounding the R^{1934} codon in N2 were tested for their genome editing activities. Briefly, plasmids carrying the guide sequence under a U6 promoter and Cas9 were transfected into MK4 cells. Cells were harvested 2 days after transfection and PCR amplification, with primers flanking the target sites, was performed on genomic DNA isolated from the transfected cells. PCR products were then subjected to T7 endonuclease I (T7E1) assay. Cleavage products generated by T7E1 are indicative of indels present in the PCR products as a result of genomic DNA breakage caused by Cas9-gRNA and the subsequent repair by NHEJ. A gRNA (g3) for Tet2 that was known to have good editing activity was included as positive control. Sixteen mice were obtained from injection of g27 (GGCATCCAGATCGGTTACA), Cas9 mRNA, and a donor oligo (shown in Fig 1, g27 underlined in blue) into 1-cell embryos. Digestion of PCR products with BglII showed that 8 contained products with the BglII site, 4 of which were homozygotes. Sequencing of PCR products confirmed that all had the correct R^{1934}A mutations. Because we mated the homozygote mice to each other, we identified potential second site mutations with the CCTop tool ([82]; https://crispr.cos.uni-heidelberg.de). g27 matches to Notch2 and to a few loci with 4 mismatches (*Lemd1*, *Ccm2*, *Papolg*, *Tubb2b* and *Tubb6*) falling within an Exon and next to a PAM sequence (no loci had fewer than 4 mismatches to this gRNA). PCR products from potential off-target sites were sequenced, and no mutations were identified in DNA isolated from any of the founders. For Notch1, a similar process led to the selection of a gRNA (CATTCGGGCATCCAGATCTG), which was injected with Cas9 mRNA and a donor oligo carrying mutations that change R^{1974} to alanine into 1-cell embryos. PCR products from 24 animals were digested with BglII and XbaI, respectively. Only 1 heterozygote founder carried the R^{1974}A mutation, confirmed by sequencing. This founder was outcrossed into our mixed colony, having a single possible 4-mismatch target in the pseudogene *Vmn1r-ps6*. In the C57BL6line, the same gRNAs were used. A single heterozygote founder pair was bred within the C57BL6line.

DSS treatment/colitis induction

For colitis induction, mice were given 1% to 2.5% DSS in autoclaved drinking water for up to 14 days. Weight was measured every day, and stool was checked for changes to monitor disease progression; in case of severe weight loss (>15%) or blood in stool, mice were euthanized. For recovery, mice were given normal drinking water for 14 days before starting the next cycle of DSS treatment, up to 4 cycles of injury and recovery. At the end of treatment, mice were euthanized, and tissue was collected for analysis.

LPS injection/dermatitis induction

To stimulate the immune system with bacterial antigens, we injected adult mice intraperitoneally twice with LPS (0.5 ug/kg bodyweight, once a month, Table 1) over an 8-week period. Blood was collected from the submandibular vein once per week to analyze IgM production by ELISA. The mice were euthanized after the eighth week and their spleens were harvested for histological analyses.

Mild dermatitis was induced by application of HDM (*Dermatophagoides farina*, Table 1) extract on the ears as described [83]. In brief, the ear lobes of adult mice were gently stripped 5 times with surgical tape and 20 ug of HDM dissolved in autoclaved PBS was administered to each ear twice weekly for 6 weeks. Mice were euthanized, and spleen harvested for histology and MZB numbers determination.

Antibodies

A full list of antibodies is provided in the Key Resource table (Table 1). The following antibodies were used for FACS analysis: Anti-mouse/human CD45R/B220, anti-CD23, anti-CD21/CD35 (CR2/CR1), anti-CD93 [AA4.1], anti-mouse IgM, anti-IgD, anti-CD45.1, anti-CD45.2, anti-CD3ε, anti-Ly-6G/Ly-6C(Gr-1), anti-CD11b, anti-TCRb, and anti-CD5 were all purchased from Biolegend. Anti-Mouse CD19 was purchased from BD Biosciences. Rabbit Anti-Ki67 (Novocastra), rabbit anti-cleaved caspase 3 (Cell signaling), rabbit anti-Phospho-Histone H3 (Ser10) (Cell signaling), rat anti-Pax5 (Biolegend), Guinea pig anti-Cytokeratin 8+18 antibody, and FITC rat anti-mouse/human CD45R/B220 (BioLegend) were used for fluorescence immunohistochemistry. Anti-rabbit Alexa Fluor Cy3 (Jackson ImmunoResearch), anti-rabbit Alexa Fluor 647 (Jackson Immunoresearch), anti-rat Cy3 (Jackson Immunoresearch), and Alexa Fluor anti-guinea pig 647 secondary antibodies were used for in fluorescence immunohistochemistry. Notch2 (D76A6) XP (Cell signaling) and HRP-linked rabbit IgG (GE healthcare) secondary antibodies were used for western blot analysis.

Protein purification and EMSA

The mouse RBPj (aa 53–474), mouse N1ICD (aa 1744–2113), mouse N1^{RA}ICD (aa 1744–2113), and human SMT3-MAML1 (aa 1–280) proteins were expressed and purified from bacteria using affinity (Ni-NTA or Glutathione), ion exchange, and/or size exclusion chromatography as previously described [84]. The purity of proteins was confirmed by SDS-PAGE with Coomassie blue staining, and concentrations were determined by absorbance measurements at UV280 with calculated extinction coefficients. EMSAs were performed using native polyacrylamide gel electrophoresis as previously described [85, 86]. Fluorescent labeled probes (1.75 nM/each probe) were mixed with increasing concentrations of purified RBPj protein in 4-fold steps (from 2.5 to 640 nM) with or without the indicated purified N1ICD and MAML proteins at 2μM. Acrylamide gels were imaged using the LICOR Odyssey CLx scanner.

Table 1. Key resources: All used materials including primer and antibodies.

Reagent or Resource	Source	Identifier
Antibodies		
Goat Anti-Mouse IgM-UNLB	Southern Biotech	1021–01
Goat Anti-Mouse IgM-HRP	Southern Biotech	1021–05
Lyophilized Rabbit Polyclonal Antibody Ki67 Antigen	Novocastra	NCL-Ki67p
Cleaved Caspase-3 (Asp175) (5A1E) Rabbit mAb	Cell signaling	9664P
Phospho-Histone H3 (Ser10) Antibody	Cell signaling	9701S
Purified anti-Pax-5 Antibody	Biolegend	649702
Cy3-AffiniPure Donkey Anti-Rabbit IgG (H+L)	Jackson ImmunoResearch	711–165–152
Cy3 AffiniPure Donkey Anti-Rat IgG (H+L)	Jackson ImmunoResearch	712–165–150
Alexa Fluor 594 anti-mouse/human CD45R/B220 [RA3-6B2]	Biolegend	103254
Anti-Metallophilic Macrophages antibody [MOMA-1]	Abcam	ab51814
Alexa Fluor 488-AffiniPure F(ab')2 Fragment Donkey Anti-Rabbit IgG (H+L)	Jackson ImmunoResearch	711–546–152
Alexa Fluor 647 anti-mouse IFN-γ [XMG1.2]	Biolegend	505816
Biotin anti-mouse IL-5 [TRFK4]	Biolegend	504401
Alexa Fluor 488 anti-mouse IL-17A [TC11-18H10.1]	Biolegend	506909
Alexa Fluor 647 anti-mouse CD3ε Antibody	Biolegend	152319
Anti-Cytokeratin 8+18 antibody (ab194130)	Abcam	ab194130
Donkey anti-Guinea Pig IgG, Alexa -2788875	Millipore Sigma	AP193SA6
Mouse NKp46/NCR1 Antibody	R&D Systems	AF2225-SP
Alexa Fluor 647 AffiniPure F(ab')₂ Fragment Donkey Anti-Goat IgG (H+L)	Jackson ImmunoResearch	705-606-147
anti-mouse/human CD45R/B220 [RA3-6B2]	Biolegend	103206
anti-mouse CD23 [B3B4]	Biolegend	103222
anti-mouse CD21/CD35 (CR2/CR1) [7E9]	Biolegend	123416
anti-mouse CD93 (AA4.1)	Biolegend	136505
anti-mouse IgM [RMM-1] 50 μg	Biolegend	406505
anti-mouse IgD [11-26c.2a]	Biolegend	405723
anti-mouse CD45.1 [A20]	Biolegend	110706
anti-mouse CD45.2 [104]	Biolegend	109814
Anti-Mouse CD3e Clone 145-2C11	BD Biosciences	553063
anti-mouse Ly-6G [1A8]	Biolegend	127615
anti-mouse/human CD11b [M1/70]	Biolegend	101216
anti-mouse/human CD45R/B220	Biolegend	103227
anti-mouse TCR β chain [H57-597]	Biolegend	109208
APC/Cy7 anti-mouse CD45R/B220	Biolegend	103224
anti-mouse CD5 [53–7.3]	Biolegend	100626
Rat Anti-Mouse CD19	Biolegend	bdb563557
CD4 Monoclonal Antibody (RM4-5), PerCP-Cyanine5.5	eBiosciences	45-0042-82

(Continued)

Table 1. (Continued)

Reagent or Resource	Source	Identifier
CD8a Monoclonal Antibody (53–6.7), FITC	eBiosciences	11-0081-82
CD8a Monoclonal Antibody (53–6.7), PE-Cyanine7	eBiosciences	25-0081-82
TCR beta Monoclonal Antibody (H57–597), APC-eFluor 780	eBiosciences	47-5961-82
APC anti-mouse CD25 Antibody (clone PC61)	Biolegend	102011
CD4 Monoclonal Antibody (GK1.5), PE	eBiosciences	12-0041-82
PE/Cy7 anti-mouse CD117 (c-Kit) Antibody	Biolegend	105814
CD3e Monoclonal Antibody (145-2C11), FITC	eBiosciences	11-0031-82
CD19 Monoclonal Antibody (eBio1D3 (1D3)), PE	eBiosciences	12-0193-82
Notch2 (D76A6) XP	Cell signaling	5732
monoclonal anti-b-actin (AC-15)	Sigma-Aldrich	A5441
ECL Rabbit IgG, HRP-linked whole AB (from Donkey)	GE Healthcare	NA934
ECL Mouse IgG, HRP-linked whole AB (from Donkey)	GE Healthcare	NA931
Bacterial and Virus Strains		
BL21 (DE3) Tuner Competent cells	Novagen	70623
Biological Samples		
Chemicals, Peptides, and Recombinant Proteins		
XbaI	NEB	R0145
BglII	NEB	R0144
Mouse IgM-UNLB	Southern Biotech	0101–01
DyLight649(Cy5)-conjugated Streptavidin	Jackson Immunoresearch	016-490-084
Dextran sulfate sodium salt (DSS, M.W. approximately 36,000–50,000, colitis grade)	MP Biomedicals	0216011050
Red blood cell lysis buffer (10x)	BioLegend	420301
BSA	Fisher Scientific	Bp1600-100
FBS	HyClone	AE24573269
FBS	Sigma-Aldrich	F2442
Nunc MaxiSorp flat bottom	Thermo Fisher Scientific	44-2404-21
TMB substrate solution	Thermo Fisher	N301
RPMI-1640	Sigma-Aldrich	R0883
Gentamicin	Gibco B.R.L	15750–060
β-mercaptoethanol	Sigma-Aldrich	M7522
U-bottom 96-well	Thermo Scientific	174925
Superfrost Plus microscope slides	Fisher Scientific	12-550-15
Xylene	Fisher Scientific	X3P
Alcian Blue 8GX	Sigma-Aldrich	A3157
Nuclear Fast Red	Vector/Sigma-Aldrich	H-3403/N3020
Trilogy	Cell Marque	920P-10
Normal donkey serum	Jackson ImmunoResearch	017-000-121

(Continued)

Table 1. (Continued)

Reagent or Resource	Source	Identifier
Prolong Gold Antifade Reagent	Invitrogen	P36930
Complete Protease Inhibitor Cocktail	Roche	11697498001
Red Blood cell lysis buffer	BioLegend	420301
ACK lysis buffer	Lonza	10-548E
Cell strainer (40 μm)	Falcon	08-771-1
Cell strainer (70 μm)	Falcon	08-771-2
Critical Commercial Assays		
Supersignal West Femto Chemiluminescent substrate kit	Thermo Scientific/Fisher Scientific	P134095
PureLink RNA Mini kit	Life Technologies (Invitrogen)	12183025
Superscript II reverse transcriptase	Invitrogen	18064014
iTaq Universal SYBR Green Supermix	Bio-Rad	1725121
Zombie VioletTM Fixable Viability kit	BioLegend	423113
Micro RNAeasy kit	Qiagen	74106
Zymo DNA Clean and Concentrator kit	Zymoresearch	D4029
Deposited Data		
SplitDam data	[45]	GEO: GSE70402
ATAC-Seq data	This paper	GEO: GSE149992
Experimental Models: Cell Lines		
mK4 cells	[93]	N/A
Experimental Models: Organisms/Strains		
N1RA	This paper	N/A
N2RA	This paper	N/A
N1 deletion	[94]	Notch1^{tm1Con}
N2 lacZ	[95]	N/A
C57BL/6	Charles River	027
FVB/N	Harlan	N/A
B6D2F2	Harlan	N/A
Oligonucleotides		
N1-deletion fwd: ACGATATCGTGGTGCATACGCTCCTGTGCG	[94]	N/A
N1-deletion rev: GTCAGTTTCATAGCCTGAAGAACG	[94]	N/A
N1RA fwd: GCGGGATTCCTAGCCTGGTTACTC	This paper	N/A
N1RA rev: GTCCTTGTTGGCTCCGTTCTTCAG	This paper	N/A
N2-LacZ fwd: GTTGCAGTGCACGGCAGATACACTTGCTGA	[95]	N/A
N2-lacZ rev: GCCACTGGTGTGTGGGCCATAATTCAATTCGC	[95]	N/A
N2RA fwd: ACGGGCTCATCCCTGACATGAG	This paper	N/A
N2RA rev: TCCTCTCAGAAGGGTAGCAAGTC	This paper	N/A
Actb qPCR fwd: GGCTGTATTCCCCTCCATCG	Harvard PrimerBank	6671509a1
Actb qPCR rev: CCAGTTGGTAACAATGCCATGT	Harvard PrimerBank	6671509a1

(Continued)

Table 1. (Continued)

Reagent or Resource	Source	Identifier
Fos qPCR fwd: CGGGTTTCAACGCCGACTA	Harvard PrimerBank	6753894a1
Fos qPCR rev: TTGGCACTAGAGACGGACAGA	Harvard PrimerBank	6753894a1
Gapdh qPCR fwd: AGGTCGGTGTGAACGGATTTG	Harvard PrimerBank	6679937a1
Gapdh qPCR rev: TGTAGACCATGTAGTTGAGGTCA	Harvard PrimerBank	6679937a1
Myb qPCR fwd: AGACCCCGACACAGCATCTA	Harvard PrimerBank	19526459a1
Myb qPCR rev: CAGCAGCCCATCGTAGTCAT	Harvard PrimerBank	19526459a1
Notch1 qPCR fwd: GATGGCCTCAATGGGTACAAG	Harvard PrimerBank	13177625a1
Notch1 qPCR rev: TCGTTGTTGTTGATGTCACAGT	Harvard PrimerBank	13177625a1
Notch2 qPCR fwd: ATGTGGACGAGTGTCTGTTGC	Harvard PrimerBank	33859592a1
Notch2 qPCR rev: GGAAGCATAGGCACAGTCATC	Harvard PrimerBank	33859592a1
Pax5 qPCR fwd: CCATCAGGACAGGACATGGAG	Harvard PrimerBank	6679213a1
Pax5 qPCR rev: GGCAAGTTCCACTATCCTTTG	Harvard PrimerBank	6679213a1
IL1b-qPCR-fwd: CAACCAACAAGTGATATTCTCCATG	[96]	N/A
IL1b-qPCR-rev: GATCCACACTCTCCAGCTGCA	[96]	N/A
IL4-qPCR-fwd: AGATGGATGTGCCAAACGTCCTCA	[97]	N/A
IL4-qPCR-rev: AATATGGGAAGCACCTTGGAAGCC	[97]	N/A
Claudin4-qPCR-fwd: GTCCTGGGAATCTCCTTGGC	Harvard PrimerBank	6753440a1
Claudin4-qPCR-rev: TCTGTGCCGTGACGATGTTG	Harvard PrimerBank	6753440a1
ZO1-qPCR-fwd: GCACCATGCCTAAAGCTGTC	[98]	N/A
ZO1-qPCR-rev: ACTCAACACACCACCATTGC	[98]	N/A
TNFa-qPCR-fwd: CCCTCACACTCAGATCATCTTCT	Harvard PrimerBank	7305585a1
TNFa-qPCR-rev: GCTACGACGTGGGCTACAG	Harvard PrimerBank	7305585a1
IL17A-qPCR-fwd: GACGCGCAAACATGAGTCC	This paper	N/A
IL17A-qPCR-rev: TTTGAGGGATGATCGCTGCT	This paper	N/A
N1RA sgRNA fwd: caccgCATTCGGGCATCCAGATCTG	This paper	N/A
N1RA sgRNA rev: aaacCAGATCTGGATGCCCGAATGc	This paper	N/A
N2RA sgRNA fwd: caccGGCATCCAGATCGGTTACA	This paper	N/A
N2RA sgRNA rev: aaacTGTAACCGATCTGGATGCC	This paper	N/A
N1RA donor oligo: g*c*t*tgcatttagatcaccctgctgaaccatcctcgcttccagatcctgctccggaacgcagctactgactagatgcccgaatgcatgatggcacaactccactgatcctggctgcggcctggccgtg*g*a*g	This paper	N/A
N2RA donor oligo: a*g*g*c*caggcgggcagccaggatcaggggggtagtaccatcgttcattctggcatccagatcgttaccgcgttgcggatcagaatctagaagagagaagcagagaagtgtccccttagataaggaaaaga*a*t*g	This paper	N/A
2xCSL(EMSA): cggaaCGTGGGAAAacctaggctagaggcacCGTGGGAAactagtgcgggcgtggct	This paper	N/A
1xSPS(EMSA): gctaCGTGGGAAAaggagcaaactgcgtTTCCCACGttccgtagtgcgggcgtggct	This paper	N/A
5'IRDye-700_complementary_oligo(EMSA): agccacgcccgcact	This paper	N/A
5'IRDye-800_complementary_oligo(EMSA): agccacgcccgcact	This paper	N/A
Recombinant DNA		
Plasmid: N1AE	[30]	N/A

(Continued)

Table 1. (Continued)

Reagent or Resource	Source	Identifier
Plasmid: N1RAΔE	This paper	N/A
pSpCas9(BB)	[99]	48139
pTXB1-Tn5	[92]	N/A
Software and Algorithms		
Image lab	Bio-Rad Laboratories	https://www.bio-rad.com/en-us/product/image-lab-software?ID=KRE6P5E8Z
Prism 8	Graph Pad	www.graphpad.com
CCTop tool	[82]	https://crispr.cos.uni-heidelberg.de
NIS-Elements Advanced Research software	Nikon	N/A
FlowJo software v9.7	Becton Dickinson	https://www.flowjo.com
Other		
LPS from *Salmonella enterica*	Sigma-Aldrich	L6143
HDM extract (*Dermatophagoisdes farina*)	Greer Laboratories Inc./Fisher Scientific	NC0277827

AB, antibody; ACK, ammonium-chloride-potassium; BSA, bovine serum albumin; CSL, CBF1/Suppressor of Hairless/LAG-1; DSS, decxtran sodium sulfate; EMSA, electrophoretic mobility shift assay; FBS, fetal bovine serum; HDM, house dust mite; HRP, horseradish peroxidase; IgG, immunoglobulin G; IgM, immunoglobulin M; LPS, lipopolysaccharide; mAb, monoclonal antibody; N1, Notch1; N1ΔE, constitutive active Notch1 lacking extracellular domain; N2, Notch2; qPCR, quantitative PCR; RA, Arg-Ala substitution; RPMI, Roswell Park Memorial Institute; sgRNA, short guide RNA; SPS, sequence-paired site; TMB, 3,3′,5,5′-Tetramethylbenzidine; UNLB, unlabeled.

https://doi.org/10.1371/journal.pbio.3000850.t001

EMSA quantitation

To quantitatively analyze the EMSA experiments, we first extracted the grayscale intensity of each band in each lane of the EMSA gels (S1A and S1B Fig). We then fitted the data to a 2-site binding model that takes into account cooperative binding to the second site. The model calculates the binding probability assuming equilibrium binding kinetics (Michaelis-Menten) to 2 sites. Cooperativity is taken into account by assuming that the binding dissociation constant of a complex to the second site is divided by a cooperativity factor C, namely that $K_{d,2nd} = \frac{1}{C} K_{d,1st}$. The probabilities to find the probe bound by 0, 1, or 2 complexes are given by

$$P_0 = \frac{1}{1 + 2\alpha + C\alpha^2}, P_1 = \frac{2\alpha}{1 + 2\alpha + C\alpha^2}, P_2 = \frac{C\alpha^2}{1 + 2\alpha + C\alpha^2}$$

where $\alpha = \frac{[NTC]}{K_d}$ is the statistical weight associated with binding of the NTC complex to a CSL site, and K_d is the dissociation constant to a single site. If the cooperativity factor, C, is equal to 1, then the binding to the 2 sites is noncooperative. $C>1$ corresponds to positive cooperativity (second binding is enhanced). $C<1$ corresponds to negative cooperativity (second binding is suppressed).

Because we observe that even at high concentrations of RBPj, the 1-site state is never depleted (e.g., see RBPj on CSL), we assumed that there is only some fraction of the probes, $f<1$, that binds 2 complexes and another fraction, $(1-f)$, that can only bind 1 complex. In this case, the probability to find the probe is modified to

$$P_0 = f \frac{1}{1 + 2\alpha + C\alpha^2} + (1-f) \frac{1}{1 + 2\alpha}, P_1 = f \frac{2\alpha}{1 + 2\alpha + C\alpha^2} + (1-f) \frac{2\alpha}{1 + 2\alpha}, P_2$$
$$= f \frac{C\alpha^2}{1 + 2\alpha + C\alpha^2}$$

We then fit the experimental data (normalized band intensities) to these expressions. The fitting parameters are K_d, C, and f. The parameters are extracted for each experiment separately.

To get an estimation of the confidence interval on the fitting parameters, we use a bootstrap method to randomly generate 5,000 data sets with the same statistical properties as the experimental data sets (the same mean and standard deviation of band intensities). We then perform the same fitting procedure on all bootstrapped data to obtain the 95% confidence interval on the fitting parameters.

Flow cytometry

For materials used, see Key resource table (Table 1). MZB and FoB cells were sorted by FACS as described in [87]. Single-cell splenocytes were prepared by placing the spleen in a petri dish and mincing it with a razor blade. The disrupted spleen tissue was then transferred into a 50-ml falcon tube and pipetted up and down in 5 ml of ice-cold 1% BSA (Fisher Scientific) in PBS and briefly vortexed to ensure thorough disruption. Single-cell suspensions were obtained by passing the disrupted spleen tissue through a 70-μm strainer (Falcon). The strainer was then rinsed with 5 ml ice-cold 1% BSA/PBS and the single-cell preparation pelleted by centrifuging at 2,000 rpm, for 5 minutes followed by red blood cell lysis (BioLegend), after which the cells were pelleted at 2,000 rpm, for 5 minutes, and resuspended in ice-cold 3% BSA in PBS before cell counting. Single-color antibody stained as well as unstained controls were prepared with 3 million splenocytes each, 1.5 μl (0.75 μg) of each antibody was added into the corresponding single-color control tube. For MZB detection, approximately 10 million cells

(in 1 ml 3% BSA) were distributed into Eppendorf tubes, and 7.5 μl of the antibody mix (2.5ul each of FITC anti-B220, PE/Cy7 anti-CD23 and PerCP/Cy5.5 anti-CD21) were added into each tube. They were then incubated at 4˚C for 60 minutes before sorting for B220$^+$CD21^{hi}CD23^{lo} MZB cells and B220$^+$CD21^{int}CD23^{hi} FoB cells. To isolate MZB (CD93$^-$B220$^+$CD19$^+$Ig-M$^+$IgD$^+$CD23^{lo}), FoB (CD93$^-$B220$^+$CD19$^+$IgM$^+$CD21$^+$), MZP (CD93$^-$B220$^+$CD19$^+$CD21^{hi}IgM^{hi}IgD^{hi}CD23^{hi}), and T2 B-cells (CD93$^+$B220$^+$IgM$^+$CD23$^+$), single-cell splenocytes were incubated with the APC/Cy7 anti-B220, PE/Cy7 anti-CD93, Hoechst blue anti-CD19, FITC anti-IgM, AmCyan anti-IgD, Percp/Cy5.5 anti-CD21 and Pacific blue CD23 and FACS sorted. To analyze peritoneal B1 B-cell populations, peritoneal cells were collected as described in [88] and incubated with APC/Cy7 anti-B220, PE anti-TCRb, FITC anti-CD11b, PE/Cy7 anti-CD23, and APC anti-CD5. They were then gated into B2 B-cells (B220$^+$CD23$^+$) and B1 B-cells (B220$^+$CD23$^-$). B1 B-cells were then gated into B1a (CD11b$^+$CD5$^+$) and B1b (CD11b$^+$CD5$^-$) B-cells.

For T-cell analysis, thymus and spleen were harvested and disrupted by gentle grinding of tissue with a pestle (CellTreat) on a 40-μm cell strainer (Falcon). Red blood cells in spleen samples were lysed using ACK lysis buffer (Lonza) for 5 minutes at 4˚C. Cells were counted and stained at 20×106 cells/ml. Cells were resuspended in PBS with Zombie Violet viability dye (Biolegend) and incubated at 4˚C for 20 minutes. Cells were washed and then resuspended in an antibody cocktail in PBS supplemented with 2% FBS (Hyclone) in the presence of 5% 2.4G2 Fc blocking antibody (in house) and incubated for 30 minutes at 4˚C. Cells were washed, resuspended in PBS with 2% FBS, and analyzed using an LSRII (BD). Data were analyzed using FlowJo software v9.7, and average population percentages and absolute numbers were graphed using GraphPad Prism (GraphPad Software, Inc.).

MZB and FoB culture and ELISA

For materials used, see Key resource table (Table 1). MZB and FoB cells were cultured in RPMI-1640 (Sigma-Aldrich) containing 10% FBS (Sigma-Aldrich), 10 μg/ml gentamicin (Gibco B.R.L) and 50 μM β-mercaptoethanol (Sigma-Aldrich). A total of 10^5 MZB and FoB cells were seeded into U-bottom 96-well plates (Thermo Scientific) in 200μL of media. Differentiation was stimulated by adding lipopolysaccharides from *Salmonella enterica* serotype typhimurium -LPS (Sigma-Aldrich) into each well at a final concentration of 2 μg/ml. The LPS-stimulated cells were cultured at 37˚C, 5% CO$_2$, for 5 days. To measure IgM levels by ELISA, MaxiSorp flat-bottom 96-well plates (Nunc) were coated with 200 μL of 5 μg/ml goat anti-mouse IgM (Southern Biotech) in 0.05% PBST (PBS-tween20) at 4˚C, overnight. The plates were then washed thrice with 0.05% PBST and blocked with 3% BSA (Fisher Scientific) in PBS for 30 minutes at room temperature. Purified mouse IgM (Southern Biotech) was used to prepare a control standard. A total of 150 μl of supernatant collected from the stimulated B-cells at the end of 5-day incubation was diluted in 0.05% PBST (PBS containing 0.05% Triton-100), and along with the standard, was loaded on to the MaxiSorp flat-bottom (Thermo Fisher Scientific) ELISA plates for 1-hour incubation at room temperature followed by 3 washes with PBST. HRP goat anti-mouse IgM (Southern Biotech), diluted at 1:5,000 in PBST, was added and incubated for 1 hour at room temperature followed by 3 washes with PBST. TMB substrate solution (Thermo Fisher Scientific) was then added and developed for 10 minutes. Development was stopped with 0.16 M sulfuric acid before colorimetric absorption analysis at 450 nm.

Histology

For materials used, see Key resource table (Table 1). Mouse tissues were fixed overnight in 4% PFA and embedded in paraffin. Adult intestinal tissue was divided into sections corresponding

to the jejunum, duodenum, ileum, and colon. Each section was then folded into a swiss-roll [89] and then fixed, mounted and sectioned for histological analysis. For P0 animals, whole intestinal tissue was collected and then fixed and mounted whole before sectioning for histological or immunofluorescence analysis. Sections 5-μm thick were deposited on Superfrost plus microscope slides (Fisher Scientific), deparaffinized with xylene (Fisher Scientific), and rehydrated. Sections were stained with hematoxylin for 2.5 minutes and Eosin for 1 minute before dehydration, clearing, and mounting. For Alcian blue staining, sections were rinsed in 3% acetic acid (Fisher Scientific) for 3 minutes and incubated at room temperature for 30 minutes in 1% Alcian blue 8GX (Sigma-Aldrich) in 3% acetic acid solution. The sections were then rinsed for 3 minutes in 3% acetic acid followed by 10 minutes in running water. After counterstaining with Nuclear Fast Red (Vector) for 5 minutes, slides were rinsed for 10 minutes in running water prior to dehydration, clearing, and mounting. For each sample, images of at least 10 random fields of view were acquired on a Nikon 90i Upright widefield microscope. Where indicated, quantitative analysis of images was done using Nikon's NIS-Elements Advanced Research software (NIS-AR). In order to automatically identify and quantify Alcian blue positive goblet cells, an inhouse NIS-AR plugin was applied to identify and mask the discrete, large, dark blue Alcian blue spots scattered on the pink-white Nuclear Fast Red counterstain (Fig 3). We then manually traced the villi in the region of interest (ROI) to exclude the Alcian blue stained mucus. The plugin then counted the Alcian blue positive foci within the ROI. Goblet cell numbers were determined for all acquired fields of view for each animal analyzed. The average number of goblet cells per field of view was obtained for each analyzed animal. Where multiple animals of the same genotype were analyzed, the average goblet cell number per field of view was obtained by averaging the goblet cell numbers in all fields of view from all the animals of that genotype.

Fluorescent immunohistochemistry

For materials used, see Key resource table (Table 1). Paraffin embedded sections were deparaffinized with xylene, rehydrated, and subjected to heat-induced epitope retrieval (HIER) by boiling in Trilogy (Cell Marque) for 30 minutes. After cooling, the sections were rinsed with distilled water for 5 minutes followed by PBS with 0.3% Triton-X100 (Fisher Scientific) for 5 minutes. The sections were then incubated at room temperature for 2 hours in blocking solution (10% normal donkey serum [Jackson ImmunoResearch] in PBS-Triton), followed by overnight incubation with respective primary antibodies at 4˚C. The sections were washed 3 times for 10 minutes each (3×10 minutes) with PBS-Triton and incubated for 2 hours at room temperature with Fluorophore-labeled secondary antibodies in blocking solution. Unbound secondary antibody was washed 3×10 minutes in PBS-Triton and where indicated, counterstained with DAPI before mounting with Prolong Gold Antifade (Invitrogen). Confocal imaging was performed on a Nikon Ti-E Inverted Microscope.

Cytoplasmic/Nuclear separation and Western Blot

For materials used, see Key resource table (Table 1). N2ICD stability was determined in FACS-isolated MZB and FoB cells. Sorted cells were pelleted for 5 minutes with 2,000 rpm at 4˚C and resuspended in 500-μl hypotonic buffer (HB; 20 mM Tris-HCl [pH 7.5], 10 mM NaCl, 3 mM MgCl$_2$) with added protease inhibitor (Roche). After 30 minutes' incubation on ice, 25 μl of 10 NP-40 was added, and samples were vortexed for 10 seconds. Nuclei were pelleted at 3,000 rpm for 10 minutes at 4˚C, and the cytoplasmic fraction transferred into a fresh tube. The nuclei pellets were washed twice in 500 μl HB and then lysed in 20 μl 2X Laemmli sample buffer (120 mM Tris-HCl [pH 6.8], 20% glycerol, 4% SDS). The cytoplasmic fractions

were concentrated using AmiconUltra– 0.5 mL– 30K centrifugal filters (Merck Millipore) and mixed 1:1 with 2X Laemmli sample buffer. The extracts were separated on 6% polyacrylamide (Bio-Rad) gel and transferred onto nitrocellulose membranes in Tris/glycine transfer buffer. Membranes were blocked with blocking solution (5% milk in 0.1% PBS-Tween20 [Fisher Scientific]) for 1 hour, room temperature, and incubated overnight at 4˚C with primary antibody in blocking solution. Membranes were then washed 3 times for 5 minutes with 0.1% PBS-Tween20 and incubated for 1 hour at room temperature with anti-rabbit HRP secondary antibody (GE healthcare) in blocking solution. Membranes were developed with a Supersignal West femto chemiluminescent substrate kit (Fisher scientific) and developed using Chemidoc (Bio-Rad) detection system. Signal intensities were quantified using Image Lab (Bio-Rad) software.

qPCR

For materials used, see Key resource table (Table 1). RNA from tissue and cells was extracted using the PureLink RNA Mini kit (Invitrogen) and cDNA was synthesized with SuperScript II reverse transcriptase (Invitrogen) following the manufacturers instruction. Quantitative PCRs were performed using iTaq Universal SYBR Green Supermix (Bio-Rad) on the StepOnePlus RT PCR system. Data were analyzed using the Delta-Delta-CT methods. A full list of oligos is provided in In Key Resources Table.

ATAC-Seq

For materials used, see Key resource table (Table 1). For sample library preparation, we followed the Omni-ATAC method outlined by [90, 91] and purified Tn5 was generated as described [92]. Briefly, 50,000 nuclei from FACS-sorted MZB cells were processed for Tn5 transposase-mediated tagmentation and adaptor incorporation at sites of accessible chromatin. FACS-isolated MZB cells were pelleted and washed with ice-cold PBS. The pellet was resuspended in ATAC-Resuspension Buffer (10 mM Tris-HCl [pH 7.4], 10 mM NaCl, 3 mM MgCl$_2$ 0.1% NP40, 0.1% Tween-20, 0.01% Digitonin) and incubated on ice for 3 minutes. The lysed cells were washed in ATAC-Wash Buffer (10 mM Tris-HCl [pH 7.4], 10 mM NaCl, 3 mM MgCl$_2$, 0.1% Tween-20), inverted 3 times, and the nuclei pelleted. The nuclei were resuspended in ATAC transposition mix (10 mM Tris-HCl [pH 7.6], 10 mM MgCl$_2$, 20% Formamide, 100 nM Tn5 transposase) and incubated at 37˚C for 30 minutes in a thermomixer at 1,000 RPM. Following tagmentation, the DNA fragments were purified using a Zymo DNA Clean and Concentrator Kit, and library amplification was performed using customized Nextera PCR primer Ad1 in combination with any of Ad2.1 through Ad2.12 barcoded primers as described [91]. The quality of the purified DNA library was performed utilizing an Agilent Bioanalyzer 2100 using High Sensitivity DNA Chips (Agilent Technologies Inc., Santa Clara, CA). The samples were pooled at a concentration of 5 nM and run on an Illumina HI-SEQ 2500 sequencer (Illumina, Inc. San Diego, CA) to obtain paired-end reads of 75 bases (PE75). ATAC sequencing was carried out on 2 conditions MZB WT and RA. For each condition, 4 biological replicates were sequenced, in single-end fashion. Read depth for replicates varied from approximately 50 to 98 million reads thereby giving us average read depth of approximately 67 million reads. Quality check, mapping, and peak calling was performed using CSBB-v3.0 [Process-ChIP-ATAC_SingleEnd]. CSBB uses fastqc, bowtie2 and macs2 [parameters:—nomodel—shift 37—extsize 73], respectively. Duplicate mapped reads were removed before peak calling. Mapped reads in bam format was converted to bigwigs using deeptools (deeptools.ie-freiburg.mpg.de) for visualization purposes. For assessing open nucleosome region differences from MZB WT to RA MZB, we performed differential peak analysis. Within each sample type, only peaks with 75% replication and at least 50% overlap among biological

replicates were used for differential peak analysis. Further, peak sets passing above defined criteria were merged (at least 1-bp overlap) using bedtools merge and then number of reads mapping under each peak for each replicate was inferred using FeatureCounts program. Finally, differential peak analysis was performed using EdgeR. No statistically significant changes in peaks (ATAC regions) between WT MZB and RA MZB were identified.

Supporting information

S1 Fig. Loss of Notch1 dimerization suppresses target gene expression in MK4 cells (S1 Fig, see S1 Data for raw data). (A-B) EMSA data for purified proteins binding to probes containing 2 CSL (A) or SPS (B) sites. The number of balls marks the occupancy of sites; arrows below indicate orientation of binding sites in probes. (C-D) The average sites filled were plotted against RBPj concentrations to calculate the cooperativity factor "C" on CSL (C) and SPS (D) probes. (E) Relative expression of Notch target genes in mK4 cells overexpressing either N1ΔE or N1^{RA}ΔE as determined by RNA Seq (all replicates are shown, values ranked per row. Green arrows indicate targets elevated more in N1^{RA}ΔE, red arrows indicate targets repressed in in N1^{RA}ΔE relative to control. (F) Luciferase activation assays were used to analyze the homo- and heterodimerization properties of Notch1 and Notch2 on a dimer-dependent reporter gene (Hes5-Luciferase) and a dimer-agnostic reporters (Hey2-Luciferase). As previously shown [38], the dimer interface involves 3 amino acids, the Arg (R) mutated in this study, as well as the positively charged Lys (K1935, Notch1) and a negatively charged Glu (E1939, Notch1, or Asp [D1899] at the equivalent position in Notch2) that form salt bridges between NICD molecules. Dimer formation is critical for Notch-dependent activation of the Hes5 reporter, and mutating any of these amino acids abrogates activation. Notably, by co-expressing 2 Notch protein with complementary mutations, one in which K1935 was changed to E (N1KE), and a second in which D1899 was changed to K (N2DK) leads to strong enhancement in Luciferase expression, explained by achieving a more favorable conformation of the complementing mutant dimer. Note synergistic complementation between N1KE and N2DK but not between N1KE and N2KD, providing strong evidence of a cooperative heterodimer. Significance tested by a Student *t*-test. CSL, CBF1/Suppressor of Hairless/LAG-1; EMSA, in electrophoretic mobility shift assay; NICD, notch intracellular domain; N1^{RA}ΔE, extracellular domain deleted Notch1 Arg^{1974}Ala mutant; RPBj, Recombinant binding protein for immunoglobulin Kappa j region; SPS, sequence-paired site.
(PDF)

S2 Fig. Normal development of T-cell compartments in *N1$^{RA/RA}$* mice (S1 Fig, see S1 Data for raw data). Thymi and spleens were isolated from *wt*, *N1$^{+/RA}$*, or *N1$^{RA/RA}$* mice, and the T-cell compartment was analyzed. (A) The absolute number of thymic single- and double-positive T cells (left) and developing T cells (right) was assessed by flow cytometry. (A') The average number of cells in the thymus (left) and average thymic weight (right) are shown. (B) The percentage (left) and absolute number (right) of T-cell subsets in the spleen were assessed by flow cytometry. (B') The average number of splenocytes (left) and average spleen weight (right) are shown. (*n* = 3–6 mice per genotype; error bars = +/- SEM). *N1$^{+/RA}$*, Notch1 Arg^{1974}Ala heterozygote; *N1$^{RA/RA}$*, Notch1 Arg^{1974}Ala homozygote; *wt*, wild-type.
(PDF)

S3 Fig. Proliferation potential in wt versus mutant intestines with or without fur mite exposure (S4 Fig). Sections of P0 and P1 intestines from animals born to fur mite–infested dams (A-H') and born after fur mite eradication (I-J') were stained for Ki67 (A-D', I, and I') and phospho-H3 (E-H', J, and J') to assess for proliferation in the crypts. *N1$^{+/-}$;N2$^{+/-}$* are

indistinguishable from *wt* (A-B', E-F'), whereas proliferation is significantly reduced in $N1^{+/-}$; $N2^{RA/RA}$ and $N1^{RA}/-;N2^{RA/-}$ crypts (C-D', G-H'). Proliferation in $N1^{RA/-};N2^{RA/-}$ is still decreased compared with heterozygous littermates after fur mite eradication (I-J'). $N1^{+/-};N2^{+/-}$, *Notch1/Notch2* RA hemizygous; $N2^{RA/RA}$, *Notch2* RA homozygous; P0-1, postnatal day 0–1; RA, Arg ($N1^{R1974}/N2^{R1934}$) to Ala substitution; wt, wild-type.
(PDF)

S4 Fig. Like wild type MZB cells, $N2^{RA/RA}$ MZB cells have a robust proliferative response upon LPS stimulation and N2RA/RA spleen display germinative centers (S5 Fig). Isolated MZB from $N2^{RA/RA}$ and *wt* littermates were cultured and stimulated with LPS. Both genotypes proliferate after stimulation (A). Sections of $N2^{RA/RA}$ and *wt* spleens were stained with Ki67 and phosphor-H3 to detect proliferation and Caspase3 for apoptosis (B). Proliferation in germinative centers were detected in dimer-deficient mice but not in *wt*. Apoptosis was not altered. LPS, lipopolysaccharide; MZB, marginal zone B-cell; *Notch2* RA homozygous; RA, Arg ($N1^{R1974}/N2^{R1934}$) to Ala substitution; wt, wild-type.
(PDF)

S5 Fig. Spleen size as a function of age. In the absence of pathogens; $N1^{+/RA};N2^{RA/RA}$ enlarged spleens and lymph nodes of mite-infested mice have a high proliferative and mitotic index (S6 Fig, see S1 Data for raw data). (A). In the absence of fur mites, an increase in spleen size with aging was observed in $N2^{RA/RA}$ mice (RA), but not in mice with other genotypes (+) housed in the same colony (B, D). The enlarged spleens and lymph nodes from aged $N1^{+/RA};N2^{RA/RA}$ mice showed increased staining for Ki67 and phosphor-H3 indicating proliferation Apoptosis was slightly increased in enlarged spleens as shown by Caspase3 stain (C). (E) Low magnification of spleens from aged $N2^{RA/RA}$ and $N1^{+/RA};N2^{RA/RA}$ mice infested with fur mites show expansion of white pulp. $N1^{+/RA};N2^{RA/RA}$, *Notch1* RA heterozygote, *Notch2* RA homozygous; RA, Arg ($N1^{R1974}/N2^{R1934}$) to Ala substitution.
(PDF)

S6 Fig. Loss of NICD dimerization does not stabilize the protein (S6 Fig; see S1 Data for raw data). Western blot analysis of nuclear (N) and cytoplasmic (C) preparations of sorted MZB shows no difference in N2 stability between *wt* and $N2^{RA/RA}$ mice (A); immunoblotting of α-tubulin and histone-h3 confirms separation of cytoplasmic and nuclear fractions, respectively. Quantification of the nuclear N2ICD relative to cytoplasmic total N2 reveals no difference between wt and dimer-deficient N2ICD stability (B). MZB, marginal zone B-cell; NICD, Notch intracellular domain; wt, wild-type.
(PDF)

S1 Table. Chi-squared analysis of pups (P0 and P1) born in of $N1^{RA/RA};N2^{RA/RA}$ x $N1^{+/-}$; $N2^{+/-}$cross in mite-free housing. N1, Notch1; N2, Notch2; RA, Arg ($N1^{R1974}/N2^{R1934}$) to Ala substitution; P, postnatal day.
(PDF)

S2 Table. Chi-squared analysis of male and female pups born in C57BL/6J $N1^{+/RA}$ x $N1^{+/RA}$ cross during fur mite infestation and following generations. $N1^{+/RA}$, Notch1 Arg[1974]Ala heterozygote.
(PDF)

S1 Data. Original images and data used to generate figures and tables presented in the manuscript, organized in tabs corresponding to figure panels.
(XLSX)

Acknowledgments

Author Contributions

Conceptualization: Eric W. Brunskill, Raphael Kopan.

Data curation: Kristina Preusse, Warren S. Pear, Rhett A. Kovall, David Sprinzak, Brian Gebelein, Eric W. Brunskill, Raphael Kopan.

Formal analysis: Francis M. Kobia, Kristina Preusse, Praneet Chaturvedi, David Sprinzak, Eric W. Brunskill, Raphael Kopan.

Funding acquisition: Raphael Kopan.

Investigation: Francis M. Kobia, Kristina Preusse, Quanhui Dai, Nicholas Weaver, Matthew R. Hass, Sarah J. Stein, Warren S. Pear, Zhenyu Yuan, Yi Kuang, Natanel Eafergen, Eric W. Brunskill.

Supervision: Kristina Preusse, Eric W. Brunskill, Raphael Kopan.

Validation: Francis M. Kobia.

Visualization: Raphael Kopan.

Writing – original draft: Francis M. Kobia.

Writing – review & editing: Kristina Preusse, Quanhui Dai, Matthew R. Hass, Rhett A. Kovall, Yi Kuang, David Sprinzak, Brian Gebelein, Eric W. Brunskill, Raphael Kopan.

References

1. Bray SJ. Notch signalling: a simple pathway becomes complex. Nat Rev Mol Cell Biol. 2006; 7(9):678–689. https://doi.org/10.1038/nrm2009 PMID: 16921404

2. Kopan R, Ilagan MX. The Canonical Notch Signaling Pathway: Unfolding the Activation Mechanism. Cell. 2009; 137(2):216–233. https://doi.org/10.1016/j.cell.2009.03.045 PMID: 19379690

3. Artavanis-Tsakonas S, Rand MD, Lake RJ. Notch signaling: cell fate control and signal integration in development. Science. 1999; 284(5415):770–776. https://doi.org/10.1126/science.284.5415.770 PMID: 10221902

4. Kovall RA, Gebelein B, Sprinzak D, Kopan R. The Canonical Notch Signaling Pathway: Structural and Biochemical Insights into Shape, Sugar, and Force. Dev Cell. 2017; 41(3):228–241. https://doi.org/10.1016/j.devcel.2017.04.001 PMID: 28486129

5. Gordon WR, Arnett KL, Blacklow SC. The molecular logic of Notch signaling—a structural and biochemical perspective. J Cell Sci. 2008; 121(Pt 19):3109–3119. https://doi.org/10.1242/jcs.035683 PMID: 18799787

6. Bray SJ. Notch signalling in context. Nat Rev Mol Cell Biol. 2016; 17(11):722–735. https://doi.org/10.1038/nrm.2016.94 PMID: 27507209

7. Masek J, Andersson ER. The developmental biology of genetic Notch disorders. Development. 2017; 144(10):1743–1763. https://doi.org/10.1242/dev.148007 PMID: 28512196

8. Aster JC, Pear WS, Blacklow SC. The Varied Roles of Notch in Cancer. Annu Rev Pathol. 2017; 12:245–275. https://doi.org/10.1146/annurev-pathol-052016-100127 PMID: 27959635

9. Siebel C, Lendahl U. Notch Signaling in Development, Tissue Homeostasis, and Disease. Physiol Rev. 2017; 97(4):1235–1294. https://doi.org/10.1152/physrev.00005.2017 PMID: 28794168

10. Radtke F, Fasnacht N, Macdonald HR. Notch signaling in the immune system. Immunity. 2010; 32 (1):14–27. https://doi.org/10.1016/j.immuni.2010.01.004 PMID: 20152168

11. Radtke F, Wilson A, Stark G, Bauer M, van Meerwijk J, MacDonald HR, et al. Deficient T cell fate specification in mice with an induced inactivation of Notch1. Immunity. 1999; 10(5):547–558. https://doi.org/10.1016/s1074-7613(00)80054-0 PMID: 10367900

12. Pui JC, Allman D, Xu L, DeRocco S, Karnell FG, Bakkour S, et al. Notch1 expression in early lymphopoiesis influences B versus T lineage determination. Immunity. 1999; 11(3):299–308. https://doi.org/10.1016/s1074-7613(00)80105-3 PMID: 10514008

13. Saito T, Chiba S, Ichikawa M, Kunisato A, Asai T, Shimizu K, et al. Notch2 is preferentially expressed in mature B cells and indispensable for marginal zone B lineage development. Immunity. 2003; 18 (5):675–685. https://doi.org/10.1016/s1074-7613(03)00111-0 PMID: 12753744

14. Maillard I, Weng AP, Carpenter AC, Rodriguez CG, Sai H, Xu L, et al. Mastermind critically regulates Notch-mediated lymphoid cell fate decisions. Blood. 2004; 104(6):1696–1702. https://doi.org/10.1182/blood-2004-02-0514 PMID: 15187027

15. Hozumi K, Negishi N, Suzuki D, Abe N, Sotomaru Y, Tamaoki N, et al. Delta-like 1 is necessary for the generation of marginal zone B cells but not T cells in vivo. Nat Immunol. 2004; 5:638–644. https://doi.org/10.1038/ni1075 PMID: 15146182

16. Witt CM, Won WJ, Hurez V, Klug CA. Notch2 haploinsufficiency results in diminished B1 B cells and a severe reduction in marginal zone B cells. J Immunol. 2003; 171(6):2783–2788. https://doi.org/10.4049/jimmunol.171.6.2783 PMID: 12960298

17. Gibb DR, El Shikh M, Kang DJ, Rowe WJ, El Sayed R, Cichy J, et al. ADAM10 is essential for Notch2-dependent marginal zone B cell development and CD23 cleavage in vivo. J Exp Med. 2010; 207 (3):623–635. https://doi.org/10.1084/jem.20091990 PMID: 20156974

18. Moran ST, Cariappa A, Liu H, Muir B, Sgroi D, Boboila C, et al. Synergism between NF-kappa B1/p50 and Notch2 during the development of marginal zone B lymphocytes. J Immunol. 2007; 179(1):195–200. https://doi.org/10.4049/jimmunol.179.1.195 PMID: 17579038

19. Tanigaki K, Han H, Yamamoto N, Tashiro K, Ikegawa M, Kuroda K, et al. Notch-RBP-J signaling is involved in cell fate determination of marginal zone B cells. Nat Immunol. 2002; 3(5):443–450. https://doi.org/10.1038/ni793 PMID: 11967543

20. Liu Z, Brunskill E, Varnum-Finney B, Zhang C, Zhang A, Jay YP, et al. The intracellular Domains of Notch1 and 2 Are Functionally Equivalent During Development and Carcinogenesis. Development. 2015; 142(14):2452–2463. https://doi.org/10.1242/dev.125492 PMID: 26062937

21. Weng AP, Ferrando AA, Lee W, Morris JP IV, Silverman LB, Sanchez-Irizarry C, et al. Activating Mutations of NOTCH1 in Human T Cell Acute Lymphoblastic Leukemia. Science. 2004; 306:269–271. https://doi.org/10.1126/science.1102160 PMID: 15472075

22. Ellisen LW, Bird J, West DC, Soreng AL, Reynolds TC, Smith SD, et al. TAN-1, the human homolog of the Drosophila notch gene, is broken by chromosomal translocations in T lymphoblastic neoplasms. Cell. 1991; 66(4):649–661. https://doi.org/10.1016/0092-8674(91)90111-b PMID: 1831692

23. Arcaini L, Rossi D, Paulli M. Splenic marginal zone lymphoma: from genetics to management. Blood. 2016; 127(17):2072–2081. https://doi.org/10.1182/blood-2015-11-624312 PMID: 26989207

24. Piris MA, Onaindia A, Mollejo M. Splenic marginal zone lymphoma. Best Pract Res Clin Haematol. 2017; 30(1–2):56–64. https://doi.org/10.1016/j.beha.2016.09.005 PMID: 28288718

25. Santos TSD, Tavares RS, Farias DLC. Splenic marginal zone lymphoma: a literature review of diagnostic and therapeutic challenges. Rev Bras Hematol Hemoter. 2017; 39(2):146–154. https://doi.org/10.1016/j.bjhh.2016.09.014 PMID: 28577652

26. Koch U, Radtke F. Notch and cancer: a double-edged sword. Cell Mol Life Sci. 2007; 64(21):2746–2762. https://doi.org/10.1007/s00018-007-7164-1 PMID: 17687513

27. Demehri S, Turkoz A, Kopan R. Epidermal Notch1 Loss Promotes Skin Tumorigenesis by Impacting the Stromal Microenvironment. Cancer Cell. 2009; 16(1):55–66. https://doi.org/10.1016/j.ccr.2009.05.016 PMID: 19573812

28. Guruharsha KG, Kankel MW, Artavanis-Tsakonas S. The Notch signalling system: recent insights into the complexity of a conserved pathway. Nat Rev Genet. 2012; 13(9):654–666. https://doi.org/10.1038/nrg3272 PMID: 22868267

29. Liu Z, Chen S, Boyle S, Ilagan MX, Zhu Y, Zhang A, et al. The Extracellular Domain of Notch2 Increases its Cell surface Abundance and Ligand Responsiveness During Kidney. Dev Cell. 2013; 25(6):585–598. https://doi.org/10.1016/j.devcel.2013.05.022 PMID: 23806616

30. Ong C, Cheng H, Chang LW, Ohtsuka T, Kageyama R, Stormo DG, et al. Target selectivity of vertebrate Notch proteins: collaboration between discrete domains and CSL binding site architecture

determine activation probability. J Biol Chem. 2006; 281(8):5106–5119. https://doi.org/10.1074/jbc.M506108200 PMID: 16365048

31. Kakuda S, Haltiwanger RS. Deciphering the Fringe-Mediated Notch Code: Identification of Activating and Inhibiting Sites Allowing Discrimination between Ligands. Dev Cell. 2017; 40(2):193–201. https://doi.org/10.1016/j.devcel.2016.12.013 PMID: 28089369

32. Haltiwanger RS. Unsweetened Notch leads to myeloproliferation. Blood. 2008; 112(2):214–215.

33. Langridge PD, Struhl G. Epsin-Dependent Ligand Endocytosis Activates Notch by Force. Cell. 2017; 171(6):1383–1396 e1312. https://doi.org/10.1016/j.cell.2017.10.048 PMID: 29195077

34. Gordon WR, Zimmerman B, He L, Miles LJ, Huang J, Tiyanont K, et al. Mechanical Allostery: Evidence for a Force Requirement in the Proteolytic Activation of Notch. Dev Cell. 2015; 33(6):729–736. https://doi.org/10.1016/j.devcel.2015.05.004 PMID: 26051539

35. Shaya O, Binshtok U, Hersch M, Rivkin D, Weinreb S, Amir-Zilberstein L, et al. Cell-Cell Contact Area Affects Notch Signaling and Notch-Dependent Patterning. Dev Cell. 2017; 40(5):505–511 e506. https://doi.org/10.1016/j.devcel.2017.02.009 PMID: 28292428

36. Sprinzak D, Lakhanpal A, LeBon L, Santat LA, Fontes ME, Anderson GA, et al. Cis Interactions beween Notch and Delta generate mutually exclusive signaling states. Nature. 2010; 465:86–90. https://doi.org/10.1038/nature08959 PMID: 20418862

37. Nandagopal N, Santat LA, LeBon L, Sprinzak D, Bronner ME, Elowitz MB. Dynamic Ligand Discrimination in the Notch Signaling Pathway. Cell. 2018; 172(4):869–880 e819. https://doi.org/10.1016/j.cell.2018.01.002 PMID: 29398116

38. Arnett KL, Hass M, McArthur DG, Ilagan MX, Aster JC, Kopan R, et al. Structural and mechanistic insights into cooperative assembly of dimeric Notch transcription complexes. Nat Struct Mol Biol. 2010; 17(11):1312–1317. https://doi.org/10.1038/nsmb.1938 PMID: 20972443

39. Bailey AM, Posakony JW. Suppressor of Hairless directly activates transcription of Enhancer of split complex genes in response to Notch receptor activity. Genes and Development. 1995; 9:2609–2622. https://doi.org/10.1101/gad.9.21.2609 PMID: 7590239

40. Nellesen DT, Lai EC, Posakony JW. Discrete enhancer elements mediate selective responsiveness of enhancer of split complex genes to common transcriptional activators. Developmental Biology. 1999; 213(1):33–53. https://doi.org/10.1006/dbio.1999.9324 PMID: 10452845

41. Nam Y, Sliz P, Pear WS, Aster JC, Blacklow SC. Cooperative assembly of higher-order Notch complexes functions as a switch to induce transcription. Proc Natl Acad Sci U S A. 2007; 104(7):2103–2108. https://doi.org/10.1073/pnas.0611092104 PMID: 17284587

42. Liu H, Chi AW, Arnett KL, Chiang MY, Xu L, Shestova O, et al. Notch dimerization is required for leukemogenesis and T-cell development. Genes Dev. 2010; 24(21):2395–2407. https://doi.org/10.1101/gad.1975210 PMID: 20935071

43. Liu F, Posakony JW. An enhancer composed of interlocking submodules controls transcriptional autoregulation of suppressor of hairless. Dev Cell. 2014; 29(1):88–101. https://doi.org/10.1016/j.devcel.2014.02.005 PMID: 24735880

44. Liu F, Posakony JW. Role of architecture in the function and specificity of two Notch-regulated transcriptional enhancer modules. PLoS Genet. 2012; 8(7):e1002796. https://doi.org/10.1371/journal.pgen.1002796 PMID: 22792075

45. Hass MR, Liow HH, Chen X, Sharma A, Inoue YU, Inoue T, et al. SpDamID: Marking DNA Bound by Protein Complexes Identifies Notch-Dimer Responsive Enhancers. Mol Cell. 2015; 59(4):685–697. https://doi.org/10.1016/j.molcel.2015.07.008 PMID: 26257285

46. Kuang Y, Golan O, Preusse K, Cain B, Salomone J, Campbell I, et al. Enhancer architecture sensitizes cell specific responses to Notch gene dose via a bind and discard mechanism. eLife. 2020; 9:e53659. https://doi.org/10.7554/eLife.53659 PMID: 32297857

47. Pellegrinet L, Rodilla V, Liu Z, Chen S, Koch U, Espinosa L, et al. Dll1- and Dll4-mediated Notch signaling is required for homeostasis of intestinal stem cells. Gastroenterology. 2011; 140(40):1230–1240.

48. Riccio O, van Gijn ME, Bezdek AC, Pellegrinet L, van Es JH, Zimber-Strobl U, et al. Loss of intestinal crypt progenitor cells owing to inactivation of both Notch1 and Notch2 is accompanied by derepression of CDK inhibitors p27(Kip1) and p57(Kip2). EMBO Rep. 2008; 9:377–383. https://doi.org/10.1038/embor.2008.7 PMID: 18274550

49. Shroyer NF, Helmrath MA, Wang VY, Antalffy B, Henning SJ, Zoghbi HY. Intestine-specific ablation of mouse atonal homolog 1 (Math1) reveals a role in cellular homeostasis. Gastroenterology. 2007; 132 (7):2478–2488. https://doi.org/10.1053/j.gastro.2007.03.047 PMID: 17570220

50. Noah TK, Shroyer NF. Notch in the intestine: regulation of homeostasis and pathogenesis. Annu Rev Physiol. 2013; 75:263–288. https://doi.org/10.1146/annurev-physiol-030212-183741 PMID: 23190077

51. Mathern DR, Laitman LE, Hovhannisyan Z, Dunkin D, Farsio S, Malik TJ, et al. Mouse and human Notch-1 regulate mucosal immune responses. Mucosal Immunol. 2014; 7(4):995–1005. https://doi.org/10.1038/mi.2013.118 PMID: 24424521

52. Obata Y, Takahashi D, Ebisawa M, Kakiguchi K, Yonemura S, Jinnohara T, et al. Epithelial cell-intrinsic Notch signaling plays an essential role in the maintenance of gut immune homeostasis. J Immunol. 2012; 188(5):2427–2436. https://doi.org/10.4049/jimmunol.1101128 PMID: 22279105

53. Okamoto R, Tsuchiya K, Nemoto Y, Akiyama J, Nakamura T, Kanai T, et al. Requirement of Notch activation during regeneration of the intestinal epithelia. Am J Physiol Gastrointest Liver Physiol. 2009; 296 (1):G23–35. https://doi.org/10.1152/ajpgi.90225.2008 PMID: 19023031

54. Nigam V, Srivastava D. Notch1 represses osteogenic pathways in aortic valve cells. J Mol Cell Cardiol. 2009; 47(6):828–834. https://doi.org/10.1016/j.yjmcc.2009.08.008 PMID: 19695258

55. Garg V, Muth AN, Ransom JF, Schluterman MK, Barnes R, King IN, et al. Mutations in NOTCH1 cause aortic valve disease. Nature. 2005; 21:180–184.

56. Vooijs M, Ong CT, Hadland B, Huppert S, Liu Z, Korving J, et al. Mapping the consequence of Notch1 proteolysis in vivo with NIP-CRE. Development. 2007; 134(3):535–544. https://doi.org/10.1242/dev.02733 PMID: 17215306

57. van Es JH, van Gijn ME, Riccio O, van den Born M, Vooijs M, Begthel H, et al. Notch/gamma-secretase inhibition turns proliferative cells in intestinal crypts and adenomas into goblet cells. Nature. 2005; 435 (7044):959–963. https://doi.org/10.1038/nature03659 PMID: 15959515

58. Carulli AJ, Keeley TM, Demitrack ES, Chung J, Maillard I, Samuelson LC. Notch receptor regulation of intestinal stem cell homeostasis and crypt regeneration. Dev Biol. 2015; 402(1):98–108. https://doi.org/10.1016/j.ydbio.2015.03.012 PMID: 25835502

59. Cerutti A, Cols M, Puga I. Marginal zone B cells: virtues of innate-like antibody-producing lymphocytes. Nat Rev Immunol. 2013; 13(2):118–132. https://doi.org/10.1038/nri3383 PMID: 23348416

60. Blaylock BL, Abdel-Nasser M, McCarty SM, Knesel JA, Tolson KM, Ferguson PW, et al. Suppression of cellular immune responses in BALB/c mice following oral exposure to permethrin. Bull Environ Contam Toxicol. 1995; 54(5):768–774. https://doi.org/10.1007/BF00206111 PMID: 7780222

61. Punareewattana K, Smith BJ, Blaylock BL, Longstreth J, Snodgrass HL, Gogal RM Jr., et al. Topical permethrin exposure inhibits antibody production and macrophage function in C57Bl/6N mice. Food Chem Toxicol. 2001; 39(2):133–139. https://doi.org/10.1016/s0278-6915(00)00116-2 PMID: 11267706

62. Quigley DA, To MD, Perez-Losada J, Pelorosso FG, Mao JH, Nagase H, et al. Genetic architecture of mouse skin inflammation and tumour susceptibility. Nature. 2009; 458(7237):505–508. https://doi.org/10.1038/nature07683 PMID: 19136944

63. Quigley DA, To MD, Kim IJ, Lin KK, Albertson DG, Sjolund J, et al. Network analysis of skin tumor progression identifies a rewired genetic architecture affecting inflammation and tumor susceptibility. Genome Biol. 2011; 12(1):R5. https://doi.org/10.1186/gb-2011-12-1-r5 PMID: 21244661

64. Peveling-Oberhag J, Wolters F, Doring C, Walter D, Sellmann L, Scholtysik R, et al. Whole exome sequencing of microdissected splenic marginal zone lymphoma: a study to discover novel tumor-specific mutations. BMC Cancer. 2015; 15:773. https://doi.org/10.1186/s12885-015-1766-z PMID: 26498442

65. Rossi D, Trifonov V, Fangazio M, Bruscaggin A, Rasi S, Spina V, et al. The coding genome of splenic marginal zone lymphoma: activation of NOTCH2 and other pathways regulating marginal zone development. J Exp Med. 2012; 209(9):1537–1551. https://doi.org/10.1084/jem.20120904 PMID: 22891273

66. Kiel MJ, Velusamy T, Betz BL, Zhao L, Weigelin HG, Chiang MY, et al. Whole-genome sequencing identifies recurrent somatic NOTCH2 mutations in splenic marginal zone lymphoma. J Exp Med. 2012; 209(9):1553–1565. https://doi.org/10.1084/jem.20120910 PMID: 22891276

67. Lefebvre C, Rajbhandari P, Alvarez MJ, Bandaru P, Lim WK, Sato M, et al. A human B-cell interactome identifies MYB and FOXM1 as master regulators of proliferation in germinal centers. Mol Syst Biol. 2010; 6:377. https://doi.org/10.1038/msb.2010.31 PMID: 20531406

68. Severson E, Arnett KL, Wang H, Zang C, Taing L, Liu H, et al. Genome-wide identification and characterization of Notch transcription complex-binding sequence-paired sites in leukemia cells. Sci Signal. 2017; 10(477).

69. Gomez-Lamarca M, Falo-Sanjuan J, Stojnic R, Abdul Rehman S, Muresan L, Jones ML, et al. Activation of the Notch Signaling Pathway In Vivo Elicits Changes in CSL Nuclear Dynamics. Dev Cell. 2018; 44(5):611–623 e617. https://doi.org/10.1016/j.devcel.2018.01.020 PMID: 29478922

70. Schroeter EH, Kisslinger JA, Kopan R. Notch-1 signalling requires ligand-induced proteolytic release of intracellular domain. Nature. 1998; 393(6683):382–386. https://doi.org/10.1038/30756 PMID: 9620803

71. Kueh HY, Yui MA, Ng KK, Pease SS, Zhang JA, Damle SS, et al. Asynchronous combinatorial action of four regulatory factors activates Bcl11b for T cell commitment. Nat Immunol. 2016; 17(8):956–965. https://doi.org/10.1038/ni.3514 PMID: 27376470

72. Falo-Sanjuan J, Lammers NC, Garcia HG, Bray SJ. Enhancer Priming Enables Fast and Sustained Transcriptional Responses to Notch Signaling. Developmental Cell. 2019; 50:1–15. https://doi.org/10.1016/j.devcel.2019.06.005 PMID: 31265808

73. Lee C, Shin H, Kimble J. Dynamics of Notch-Dependent Transcriptional Bursting in Its Native Context. Dev Cell. 2019; 50(4):426–435 e424. https://doi.org/10.1016/j.devcel.2019.07.001 PMID: 31378588

74. Cave JW, Loh F, Surpris JW, Xia L, Caudy MA. A DNA transcription code for cell-specific gene activation by notch signaling. Curr Biol. 2005; 15(2):94–104. https://doi.org/10.1016/j.cub.2004.12.070 PMID: 15668164

75. MacGrogan D, Nus M, de la Pompa JL. Notch signaling in cardiac development and disease. Curr Top Dev Biol. 2010; 92:333–365. https://doi.org/10.1016/S0070-2153(10)92011-5 PMID: 20816401

76. Donovan J, Kordylewska A, Jan YN, Utset MF. Tetralogy of fallot and other congenital heart defects in Hey2 mutant mice. Curr Biol. 2002; 12(18):1605–1610. https://doi.org/10.1016/s0960-9822(02)01149-1 PMID: 12372254

77. Sakata Y, Kamei CN, Nakagami H, Bronson R, Liao JK, Chin MT. Ventricular septal defect and cardiomyopathy in mice lacking the transcription factor CHF1/Hey2. Proc Natl Acad Sci U S A. 2002; 99 (25):16197–16202. https://doi.org/10.1073/pnas.252648999 PMID: 12454287

78. Huang CH, Kuo IC, Xu H, Lee YS, Chua KY. Mite allergen induces allergic dermatitis with concomitant neurogenic inflammation in mouse. J Invest Dermatol. 2003; 121(2):289–293. https://doi.org/10.1046/j.1523-1747.2003.12356.x PMID: 12880420

79. Johnston NA, Trammell RA, Ball-Kell S, Verhulst S, Toth LA. Assessment of immune activation in mice before and after eradication of mite infestation. J Am Assoc Lab Anim Sci. 2009; 48(4):371–377. PMID: 19653944

80. Pochanke V, Hatak S, Hengartner H, Zinkernagel RM, McCoy KD. Induction of IgE and allergic-type responses in fur mite-infested mice. Eur J Immunol. 2006; 36(9):2434–2445. https://doi.org/10.1002/eji.200635949 PMID: 16909433

81. Moats CR, Baxter VK, Pate NM, Watson J. Ectoparasite Burden, Clinical Disease, and Immune Responses throughout Fur Mite (Myocoptes musculinus) Infestation in C57BL/6 and Rag1(-/-) Mice. Comp Med. 2016; 66(3):197–207. PMID: 27298244

82. Stemmer M, Thumberger T, del Sol Keyer M, Wittbrodt J, Mateo JL. CCTop: An Intuitive, Flexible and Reliable CRISPR/Cas9 Target Prediction Tool. PLoS ONE. 2015; 10(4):e0124633. https://doi.org/10.1371/journal.pone.0124633 PMID: 25909470

83. Jin M, Choi JK, Choi YA, Kim YY, Baek MC, Lee BH, et al. 1,2,4,5-Tetramethoxybenzene Suppresses House Dust Mite-Induced Allergic Inflammation in BALB/c Mice. Int Arch Allergy Immunol. 2016; 170 (1):35–45. https://doi.org/10.1159/000446510 PMID: 27355819

84. Friedmann DR, Wilson JJ, Kovall RAJJoBC. RAM-induced allostery facilitates assembly of a notch pathway active transcription complex. 2008; 283(21):14781–14791. https://doi.org/10.1074/jbc.M709501200 PMID: 18381292

85. Uhl JD, Cook TA, Gebelein B. Comparing anterior and posterior Hox complex formation reveals guidelines for predicting cis-regulatory elements. Developmental Biology. 2010; 343:154–166. https://doi.org/10.1016/j.ydbio.2010.04.004 PMID: 20398649

86. Uhl JD, Zandvakili A, Gebelein B. A Hox Transcription Factor Collective Binds a Highly Conserved Distal-less cis-Regulatory Module to Generate Robust Transcriptional Outcomes. PLoS Genet. 2016; 12 (4):e1005981. https://doi.org/10.1371/journal.pgen.1005981 PMID: 27058369

87. Chen TT, Tsai MH, Kung JT, Lin KI, Decker T, Lee CK. STAT1 regulates marginal zone B cell differentiation in response to inflammation and infection with blood-borne bacteria. J Exp Med. 2016; 213 (13):3025–3039. https://doi.org/10.1084/jem.20151620 PMID: 27849553

88. Ray A, Dittel BN. Isolation of mouse peritoneal cavity cells. J Vis Exp. 2010;(35).

89. Moolenbeek C, Ruitenberg EJ. The "Swiss roll": a simple technique for histological studies of the rodent intestine. Lab Anim. 1981; 15(1):57–59. https://doi.org/10.1258/002367781780958577 PMID: 7022018

90. Corces MR, Trevino AE, Hamilton EG, Greenside PG, Sinnott-Armstrong NA, Vesuna S, et al. An improved ATAC-seq protocol reduces background and enables interrogation of frozen tissues. Nat Methods. 2017; 14(10):959–962. https://doi.org/10.1038/nmeth.4396 PMID: 28846090

91. Buenrostro JD, Wu B, Chang HY, Greenleaf WJ. ATAC-seq: A Method for Assaying Chromatin Accessibility Genome-Wide. Curr Protoc Mol Biol. 2015; 109:21.29.1–21.29.9.

92. Picelli S, Bjorklund AK, Reinius B, Sagasser S, Winberg G, Sandberg R. Tn5 transposase and tagmentation procedures for massively scaled sequencing projects. Genome Res. 2014; 24(12):2033–2040. https://doi.org/10.1101/gr.177881.114 PMID: 25079858

93. Valerius MT, Patterson LT, Witte DP, Potter SS. Microarray analysis of novel cell lines representing two stages of metanephric mesenchyme differentiation. Mech Dev. 2002; 110(1–2):151–164. https://doi.org/10.1016/s0925-4773(01)00581-0 PMID: 11744376

94. Conlon RA, Reaume AG, Rossant J. Notch1 is required for the coordinate segmentation of somites. Development. 1995; 121(5):1533–1545. PMID: 7789282

95. Skarnes WC, Moss JE, Hurtley SM, Beddington RSP. Capturing Genes Encoding Membrane and Secreted Proteins Important For Mouse Development. Proc Natl Acad Sci U S A. 1995; 92(14):6592–6596. https://doi.org/10.1073/pnas.92.14.6592 PMID: 7604039

96. Cao SS, Song B, Kaufman RJ. PKR protects colonic epithelium against colitis through the unfolded protein response and prosurvival signaling. Inflammatory bowel diseases. 2012; 18(9):1735–1742. https://doi.org/10.1002/ibd.22878 PMID: 22275310

97. Stellato C, Gubin MM, Magee JD, Fang X, Fan J, Tartar DM, et al. Coordinate Regulation of GATA-3 and Th2 Cytokine Gene Expression by the RNA-Binding Protein HuR. The Journal of Immunology. 2011:1001881.

98. Chihara M, Ikebuchi R, Otsuka S, Ichii O, Hashimoto Y, Suzuki A, et al. Mice Stage-Specific Claudin 3 Expression Regulates Progression of Meiosis in Early Stage Spermatocytes1. Biology of Reproduction. 2013; 89(1).

99. Ran FA, Hsu PD, Wright J, Agarwala V, Scott DA, Zhang F. Genome engineering using the CRISPR-Cas9 system. Nature Protocols. 2013; 8(11):2281–2308. https://doi.org/10.1038/nprot.2013.143 PMID: 24157548